Multiscale Modeling of In-Room Temperature Distribution with Human Occupancy Data: A Practical Case Study

Yohei Kono,[1] Yoshihiko Susuki,[1, 2] Mitsunori Hayashida,[3] Igor Mezić,[4] and Takashi Hikihara[1]
[1]*Department of Electrical Engineering, Kyoto University, Kyoto, Japan*
[2]*JST-CREST, Saitama, Japan*
[3]*Environmental Solutions Business Headquarters, OMRON Corporation, Kyoto, Japan*
[4]*Department of Mechanical Engineering, University of California, Santa Barbara, USA*

This paper develops a method for modeling of in-room temperature distribution incorporated with data collected by human sensors. This modeling is based on a standard two-dimensional heat diffusion equation with an effective diffusion coefficient. The effective diffusion coefficient is nominally identified from characteristics of air flow inside a room and its architectural design. For modeling multiple time-scale influence of human occupancy on the in-room temperature distribution, two independent parameters—the effective diffusion coefficient and human heat input—of the equation are modulated with the human sensor data that capture spatio-temporal dynamics of the occupancy in high resolution. The developed method is applied to a practical office space in commercial building in Japan so that its effectiveness is demonstrated by comparing numerical simulations of the equation with measured data on temperature.

Keywords: in-room temperature distribution; human sensor data; modeling; effective diffusion coefficient; multiscale

I. INTRODUCTION

In-building energy dynamics occur on a wide range of scales in both space and time. For their representation, two different types of mathematical models have been used in literature. First, lumped-parameter models are used in order to predict and control coarse-scale thermal dynamics: see e.g. [1]—ranges of more than lengths between rooms and hours. Second, distributed-parameter models have been developed for fine-scale thermal dynamics inside a room. For example, Ren and Stewart [2] proposed a mathematical model of temperature distribution inside a building described by equations of temperature and air flow volume in sub-zones into which a room is divided. Zhang, *et al.* [3] represented the distribution of in-room temperature as a linear superposition of temperature changes caused by individual heat sources or sinks, where the temperature changes were identified with Computational Fluid Dynamics (CFD) program. Osawa, *et al.* [4] proposed to incorporate a lumped-parameter model, which represented coarse-scale in-room thermal dynamics, with a fine-scale advective transport term by the air flow close to ceiling.

The fine-scale modeling has two main advantages for analysis and design of various HVAC systems. The first is a better comprehension of undesirable phenomena of the HVAC systems. One of the phenomena is the so-called *hunting* behavior [5] in which an undesired oscillation of in-room temperature field develops. This behavior is often observed in a building with dispersed multiple HVAC units and is caused by not only their nonlinear characteristics, an oscillatory response of thermal loads but also a dynamic thermal interaction of neighboring HVAC units. The fine-scale modeling effectively describes the thermal interaction as a dynamic response of in-room temperature field driven by heat inputs from the HVAC units. By using this description, it becomes possible to capture the underlying mechanism of the hunting behavior and eliminate it in design and operational stages of the HVAC systems. The second is an effective design of the HVAC management with taking human occupancy into account. The consumption of energy for air conditioning can be saved by setting the rates of ventilation based on human occupancy. The idea is widely known as the *demand-controlled ventilation*: see e.g. [6, 7]. Indeed, new management technologies of the HVAC systems are proposed by using information on human occupancy collected by sensors or predicted by models [8, 9]. The management technologies contribute to local and precise control of in-room temperature without any disturbance to human activity. Here, the sort of control involves multiple HVAC units that are operated in a coordinated manner. As stated above, their coordination might cause the hunting behavior. Thus, in the coordination, it is required to precisely regulate the in-room temperature while suppressing the hunting behavior. A possible idea for this is to *nowcast* (namely, predict in a very short-time horizon) the time response of in-room temperature and to use it for determining control efforts of the HVAC units. The idea is realized by the fine-scale modeling via the so-called model predictive control [10] that has been reported for control of in-building thermal dynamics [11, 12].

In this paper, we focus on a room used for office space with the following two features. First, the ceiling height of room is about three meters and much smaller than both its length and width. Thus, the thermal dynamics in the vertical (height) direction are steady and simply described, while the dynamics in the horizontal (length and width) direction are modeled in detail. Second, human occupancy is measured in both space and time. The measurement is feasible with infrared ray sensors [13], whose resolutions are less than 2.6 m in space and 1 s in time. The sensor technology is promising and makes it possible to derive highly-resolved data on human occupancy in remote. It is expected that the highly-resolved data are used for local and energy-efficient control of the HVAC systems: see as similar ideas [14, 15].

An important problem posed here is how the highly-resolved data on human occupancy are exploited for estimating fine-scale temperature distribution in a room. Generally speaking, it is difficult to directly derive highly-resolved data on in-room temperature because of the following reasons. For the space-resolution, air temperature can not be remotely measured, and dense spatial deployment of temperature sensors is feasible only in the stage of architectural design. For the time-resolution, time constants of temperature sensors are of order of minutes [16], which are larger than the time constants of human sensor mentioned above. Thus, it is impossible to sample in-room thermal dynamics faster than the time constants of temperature sensors. From these, it is necessary to explore the modeling of fine-scale temperature distribution based on available measurement data.

The purpose of this paper is to develop a method for fine-scale modeling of in-room temperature distribution incorporated with highly-resolved human occupancy data. To do this, it is required to consider two problems unsolved in literature. The first problem is to evaluate beyond the CFD capacity how a complex air motion affects the temperature distribution. Normal CFD is time-consuming and computationally burdening. It has been widely acknowledged that CFD is not suitable to real-time control and low-latency communication of in-building devices. Moreover, CFD is not suitable to capturing the underlying mechanism of the hunting behavior because CFD's outputs, including all the turbulent effects coupled with the complex air motion, are too intricate to clearly quantify the dynamic interaction of neighboring HVAC units. The second is to model how the spatio-temporal dynamics of human occupancy affect the in-room temperature distribution. Human occupants work as not only rapidly mobile heat sources but also obstacle objects. The dynamics of mobile occupants affect the temperature distribution and possibly induce the hunting behavior. However, CFD is unable to predict the dynamic effect because mobile occupants determine geometry and boundary conditions in a CFD simulation that vary in space and time. That is to say, the mobile occupants require a completely different CFD project at every onset when one occupant moves in space. This is a computationally impossible task in the case of a large number of occupants. Thus, the local and precise control of in-room temperature needs a novel idea in accurate and simple modeling of the dynamic effect without CFD. By considering these, in this paper we newly propose to use a mathematical model of in-room thermal dynamics without inclusion of CFD and to incorporate the model with highly-resolved data on human occupancy. In particular, we describe the incorporation by applying it to a practical office space in a commercial building, where the human occupancy data are available. A preliminary version of this work is published as our non-reviewed technical report [17].

The contributions of this paper are two-fold. First, we treat the advective heat transfer in the office using a two-dimensional, isotropic diffusion equation that accurately and simply describes the air motion [18]. This treatment is widely known in fluid mechanics as the *effective diffusion* or *eddy diffusion*: see e.g. [19, 20]. It enables the fast prediction of in-room temperature and provides a simple description of the dynamic response of temperature field driven by a heat input. Second, we model the influence of human occupancy on in-room temperature as spatio-temporal modulations of the effective coefficient and heat source term in the diffusion equation. The influence modeled here is *multiscale* in space and time: globally slow effect due to a human occupant as an external heat source and locally fast effect due to an air motion around the occupant. Our modulation idea is different from the conventional one that the influence of stationary human occupants is quantified with CFD programs [3, 21, 22]. The proposed description with the space- and time-dependent coefficient is applicable to quantifying in-room thermal dynamics driven by the so-called *Variable Air Volume* (VAV) units [23]. A procedure of modulating the effective coefficient and heat source term with human occupancy data is investigated and established with the Proper Orthonormal Decomposition (POD) [24] in order to archive a physically relevant and computationally efficient description of the target dynamic phenomenon.

The rest of this paper is structured as follows. Sec. II provides basic information on modeling target in the commercial building. In Sec. III we propose a method for modeling of in-room temperature distribution incorporated with measurement of human occupancy. A procedure of how to numerically implement the proposed modeling for the target office space is described in Sec. IV. In Sec. V, we perform numerical simulations for the target space and evaluate the proposed modeling by comparison of numerical and measured data. Sec. VI is the conclusion of this paper with a summary and future prospects.

II. MODELING TARGET IN COMMERCIAL BUILDING

This paper focuses on a practically used office space in a commercial building in order to delineate the modeling idea. This room is located in the main building of OMRON Healthcare Co., Ltd. in Kyoto, Japan. This section provides basic information on the room as the modeling object: spatial arrangements and operational conditions of HVAC units, and measurement of temperature and human occupancy.

Figures 1(a) and (b) show a photograph and two-dimensional geometry of the modeling object. The area surrounded with the red *broken* lines in Fig. 1(b) represents the target space for the current modeling. The

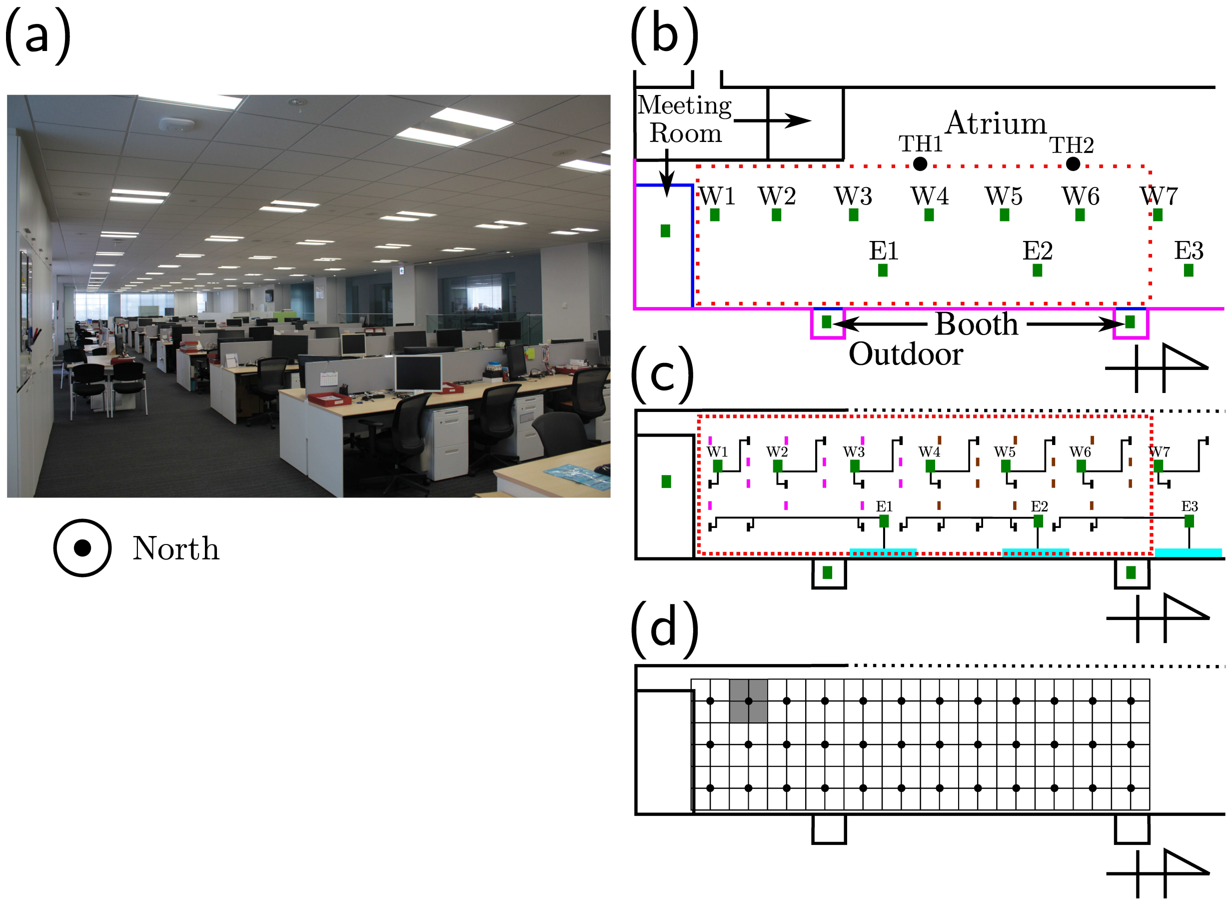

FIG. 1. (a) Photograph of modeling object. (b) Geometry of modeling object in the commercial building. The target space for the current modeling corresponds to the area surrounded with the red *broken* lines. The blue lines stand for glass walls, the black lines for normal walls, and the purple lines for outer walls with glass-windows. The green rectangular symbols stand for the positions of task-units, and the black circle symbols for temperature sensors. Task-units are called W1 to W7 and E1 to E3, and temperature sensors called TH1 and TH2. (c) Outlet and intake ducts of HVAC units in the office. The black rectangular symbols stand for outlet ducts of task-units, the green rectangular for intake ducts of W1 to W7, and the cyan rectangular for intake ducts of E1 to E3. The purple and brown rectangular symbols stand for outlet ducts of ambient-units. (d) Thermal occupant detector sensors and their 144 detection areas in the target space. The dot symbols stand for the sensors. As shown as the shaded areas, four rectangles around each sensor stand for its detection areas.

size of the space is approximately 40 m (length: south-to-north) × 10 m (width: west-to-east) × 2.8 m (height). The eastern boundary of the space corresponds to the outer walls of the building or the glass walls on booths, denoted by the purple and blue *solid* lines, respectively. The southern boundary is the glass wall next to a meeting room. The southern part of the western boundary is the wall separating the target space from a meeting room, and its northern part is faced to the atrium. There is no wall on the northern boundary faced to the other office space.

Next, we review spatial arrangements and operational conditions of HVAC units. The target space has two types of HVAC units for conditioning *locally* and *globally* in space, called *task*-units and *ambient*-units, respectively. The task-units are denoted by the green rectangular symbols in Fig. 1(b), and named W1 to W7 and E1 to E3. The outlet ducts of task-units are denoted by the black rectangular symbols in Fig. 1(c). The intake ducts of W1 to W7 are placed on the ceiling, which are denoted by the green rectangular symbols in Fig. 1(c). The intake ducts of E1 to E3 are placed on the wall, which are denoted by the cyan rectangular symbols in Fig. 1(c). Also, the two ambient-units are placed in the target space. These outlet ducts are denoted by the purple and brown rectangular symbols in Fig. 1(c). Table I shows operational conditions of HVAC units. The HVAC units run on a programmed schedule. Different reference values of in-room temperature are set for the task- and ambient-units. The setting values of outlet volume are also different. Outlet temperature of ambient-units was sampled, and that of task-units was not sampled.

Finally, we review the measurement system of temperature and human occupancy in the target space. All the

TABLE I. Operational conditions of HVAC units for the target office space.

	Running period	Temp. reference	Outlet volume setting	Outlet temp.
Task (W1 to W7)	8:00–22:00	28 °C	$0.15\,\mathrm{m}^3/\mathrm{s}$	Not measured
Task (E1 to E3)	8:00–22:00	28 °C	$0.22\,\mathrm{m}^3/\mathrm{s}$	Not measured
Ambient	7:30–17:35	26 °C	$0.94\,\mathrm{m}^3/\mathrm{s}$	Measured

temperature data were sampled by 0.1 °C every 10 minutes. Temperature sensors used for the sampling include an NTC thermistor. In-room temperature was measured in the intake ducts of task-units W1 to W7. Temperature in the meeting room and booths was measured as well as by W1 to W7. Besides, temperature sensors, which are denoted by the circle symbols in Fig. 1(b), are placed at the height 1.5 m above the floor and measure temperature near the atrium. Moreover, outdoor temperature was also sampled. Human occupancy was sampled in 144 rectangles every 1 second by thermal occupant detector sensors on the ceiling. The detector sensors in this space include an infrared ray sensor module manufactured by OMRON Corporation. Mechanism and performance of the sensors are similar to [13]. The detection areas of every sensor are shown in Fig. 1(d). The size of each rectangle is 1.8 m × 1.8 m. If anyone stays in one of four rectangles, then the corresponding sensor outputs unity; otherwise, it outputs null. For the current fine-scale modeling of temperature, we use data obtained by highly-resolved measurement of human occupancy. The data on coarse-scale measurement of in-room temperature are used for evaluating the current modeling and determining a boundary condition of the equation derived in the next section.

III. PROPOSED FRAMEWORK OF IN-ROOM TEMPERATURE MODELING

This section contains the main idea of this paper and proposes a method for modeling of in-room temperature distribution based on the incorporation of heat diffusion equation with measured data on human occupancy.

A. Mathematical modeling of heat diffusion

First of all, we introduce a mathematical model of in-room temperature distribution based on fluid and thermal physics. In the target space denoted by $S \subset \mathbb{R}^3$, the dynamics of temperature $T(\boldsymbol{r}, t)$ at position $\boldsymbol{r}$ and time t are represented by the following energy equation [1]:

$$\frac{\partial}{\partial t}T(\boldsymbol{r},t) + \boldsymbol{u}(\boldsymbol{r},t)\cdot\boldsymbol{\nabla}_r T(\boldsymbol{r},t) = D\Delta_r T(\boldsymbol{r},t) + \frac{P(\boldsymbol{r},t)}{\rho c_\mathrm{p}}, \quad \boldsymbol{r} \in S \subset \mathbb{R}^3,\ t \in \mathbb{R}, \tag{1}$$

where D is the thermal molecular diffusion coefficient of air, $\boldsymbol{u}(\boldsymbol{r}, t)$ is the air velocity field in the target space, $\boldsymbol{\nabla}_r$ is the vector differential operator in Cartesian coordinates $\boldsymbol{r}$, $\Delta_r = \boldsymbol{\nabla}_r \cdot \boldsymbol{\nabla}_r$ is the Laplacian operator, ρ and c_p are the density and the specific heat at constant pressure. Also, $P(\boldsymbol{r}, t)$ stands for the heat input per unit time and volume from indoor and outdoor sources. The second term of the left-hand side of Eq. (1) represents the advective heat transfer. Note that the advective transfer has been commonly analyzed by CFD programs: see e.g. [3, 22].

As mentioned in Sec. I, in this paper we focus on two-dimensional thermal dynamics in the horizontal direction. To do this explicitly, let us decompose the temperature distribution $T(\boldsymbol{r}, t)$ into the two functions of length x, width y, height z, and time t as follows:

$$T(\boldsymbol{r},t) = T^\mathrm{H}(x,y,t) + T^\mathrm{V}(z). \tag{2}$$

The first function $T^\mathrm{H}(x, y, t)$ represents the thermal dynamics in the horizontal direction and is modeled in the next paragraph. The second function $T^\mathrm{V}(z)$ represents the steady temperature profile in the vertical (height) direction. Eq. (2) is valid when the vertical distribution of in-room temperature is uniform in the horizontal direction and time. This assumption is widely adopted: see e.g. [16, 25]. By considering the standard profile in which air temperature increases with height (see Fig. 3 in detail), we simply formulate $T^\mathrm{V}(z)$ as the following linear function:

$$T^\mathrm{V}(z) = c\left(z - \frac{h}{2}\right),\ z \in [0,h], \tag{3}$$

where c is the coefficient characterizing the temperature profile in height and will be determined from the measurement in Sec. IV B. Also, h is the height of the target space.

Now, we propose a simple representation of the advective heat transfer without CFD program and thereby formulate the spatio-temporal evolution of $T^\mathrm{H}(x, y, t)$. Let $\Omega \subset \mathbb{R}^3$ and $\mathcal{I} \subset \mathbb{R}$ be closed domain and interval used for coarse-graining of advective transfer phenomena in a scalar field. We assume that the standard advection-diffusion equation such as Eq. (1) satisfies the following condition:

$$\int_{\Omega\times\mathcal{I}} \boldsymbol{u}(\boldsymbol{r},t)\mathrm{d}x\mathrm{d}y\mathrm{d}z\mathrm{d}t = \boldsymbol{0}. \tag{4}$$

Then, it is shown in [18] that under this condition, the advection-diffusion equation is approximated (coarse-grained) by a diffusion equation on length- and time-scales larger than the size of $\Omega \times \mathcal{I}$. This provides a theoretical basis of our modeling, called the *homogenization* [18]. The condition (4) suggests that the air flow $\boldsymbol{u}$ changes on the scales smaller than the size of $\Omega \times \mathcal{I}$. This is valid in various indoor situations that are well-conditioned and applicable to practically used office space. In such a situation, the temperature gradient is so small that the buoyancy-driven flow does not circulate globally. Also, the Reynolds number is so large that the time-varying component of the flow is rapidly damped due to the air viscosity (see Sec. IV A in detail). Thus, it is relevant to represent the heat transfer as the diffusion phenomenon. By considering space- and time-fluctuation of the flow's state over the size of $\Omega \times \mathcal{I}$, we introduce a scalar function D_{eff} on position (x, y) and time t in order to describe the diffusion phenomenon. The function D_{eff} is called *effective diffusion coefficient* in this paper. Note that we have assumed the diffusion phenomenon as an isotropic one due to the outlet ducts symmetrically located in length and width. Hence, the following partial differential equation is derived for the two-dimensional closed domain A of the target space S:

$$\begin{aligned} \frac{\partial}{\partial t} T^{\mathrm{H}}(\boldsymbol{x}, t) =& D_{\mathrm{eff}}(\boldsymbol{x}, t) \Delta T^{\mathrm{H}}(\boldsymbol{x}, t) + \frac{P(\boldsymbol{x}, t)}{\rho c_{\mathrm{p}}}, \\ & \boldsymbol{x} := (x, y) \in A \subset \mathbb{R}^2, \end{aligned} \tag{5}$$

where Δ stands for the Laplacian operator with respect to $\boldsymbol{x} = (x, y)$. The heat input term $P(\boldsymbol{x}, t)$ is decomposed with assuming their simple superposition as follows:

$$\begin{aligned} P(\boldsymbol{x}, t) =& P_{\mathrm{HVAC}}(\boldsymbol{x}, t) + P_{\mathrm{conv}}(\boldsymbol{x}, t) + P_{\mathrm{rad}}(\boldsymbol{x}, t) \\ & + P_{\mathrm{solar}}(\boldsymbol{x}, t) + P_{\mathrm{eqp}}(\boldsymbol{x}, t) + P_{\mathrm{human}}(\boldsymbol{x}, t), \end{aligned} \tag{6}$$

where $P_{\mathrm{HVAC}}(\boldsymbol{x}, t)$ stands for the heat input from the outlet ducts, $P_{\mathrm{conv}}(\boldsymbol{x}, t)$ for the convective heat transfer from indoor walls, $P_{\mathrm{rad}}(\boldsymbol{x}, t)$ for the thermal radiation from indoor walls, $P_{\mathrm{solar}}(\boldsymbol{x}, t)$, $P_{\mathrm{eqp}}(\boldsymbol{x}, t)$, and $P_{\mathrm{human}}(\boldsymbol{x}, t)$ for the heat inputs from solar radiation, office equipment, and human occupants in the target space, respectively. These heat sources are modeled as discretized forms in Sec. IV C.

In addition to the thermal dynamics, we model the influence of human occupancy on temperature distribution. A human occupant works as not only a heat source affecting the thermal dynamics but also a mobile body affecting the fluid motion in the office [26]. We call these effects the *thermal effect* and *fluid effect*, respectively. These effects control the in-room temperature distribution in different time-scales: the thermal effect works more slowly than the fluid effect because the time constant of convective heat transfer from a human occupant is larger than that of human movement. Here, the fluid effect is a short time-scale phenomenon and cannot be modeled by the above homogenization on the target time-scale. Thus, the effect needs the incorporation of time-dependency in D_{eff} (see Sec. IV A). In this paper, we represent the multiscale influence as spatio-temporal modulations of P_{human} and D_{eff} controlled by human occupancy (see Sec. III B). The occupancy is represented by a distribution function $N(\boldsymbol{x}, t)$, which is obtained in a discretized manner from measured data on human occupancy (see Sec. IV D).

Here, we note the difference between the two models (1) and (5) from the viewpoint of HVAC design and operation. Eq. (1) fully describes the in-room thermal dynamics coupled with micro- and macro-scale fluid motions. On the other hand, the proposed model (5) implies a homogenization of the thermal dynamics modeled as a macro-scale heat diffusion, thereby formulating the thermal interaction of multiple HVAC units as the dynamic response of temperature field $T(\boldsymbol{x}, t)$ driven by the heat input $P(\boldsymbol{x}, t)$. Hence, Eq. (5) provides a simple description of the hunting behavior and is suitable to the coordination design of multiple HVAC units.

B. Data-assisted modeling of human effects

This subsection introduces a data-assisted formulation of P_{human} and D_{eff} for representation of both thermal and fluid effects.

1. *Input heat term* P_{human}

Suppose that a single human occupant works as a constant heat source denoted by P_0 at sensing duration. Then, it is natural to describe $P_{\mathrm{human}}(\boldsymbol{x}, t)$ as the following function:

$$P_{\mathrm{human}}(\boldsymbol{x}, t) := P_0 N(\boldsymbol{x}, t). \tag{7}$$

The coefficient P_0 will be determined with discretization for numerical implementation in Sec. IV C 5.

2. *Effective diffusion coefficient* D_{eff}

When no occupant in the target space, we assume that D_{eff} is a time-invariant function $D_{\mathrm{eff}}^{(0)}(\boldsymbol{x})$. This is valid for the office space in Sec. II because the outlet volume is set at a constant value and does not change drastically in time. Note that D_{eff} becomes a time-varying function when multiple VAV units are operated in an office space (see App. A). In the following, we consider two mechanisms of spatio-temporal modulation of $D_{\mathrm{eff}}^{(0)}(\boldsymbol{x})$ by $N(\boldsymbol{x}, t)$.

The first mechanism is related to non-zero volume of human body. Consider a small decrease of volume around position $\boldsymbol{x}$ and at time t, $V - V_{\mathrm{human}} N(\boldsymbol{x}, t)$, where V is the original volume around $\boldsymbol{x}$ and V_{human} the averaged volume of human body. By assuming that the human body is encompassed by an adiabatic surface (or thermal insulator) [3, 27], and by considering the heat balance in the small volume, we approximately re-write the heat diffusion equation (5) as follows:

$$\begin{aligned}\{V - V_{\mathrm{human}}N(\boldsymbol{x},t)\}\frac{\partial}{\partial t}T^{\mathrm{H}}(\boldsymbol{x},t) = \\ VD^{(0)}_{\mathrm{eff}}(\boldsymbol{x})\Delta T^{\mathrm{H}}(\boldsymbol{x},t) \\ + \{V - V_{\mathrm{human}}N(\boldsymbol{x},t)\}\frac{P(\boldsymbol{x},t)}{\rho c_{\mathrm{p}}},\end{aligned} \tag{8}$$

where the density of air is assumed to be constant. The assumption is relevant when the volume V_{human} of human body is much smaller than the original volume V. The human-body effect is hence represented as the following modulation D_{vol} of $D^{(0)}_{\mathrm{eff}}$:

$$D_{\mathrm{vol}}(\boldsymbol{x},t) := \frac{V}{V - V_{\mathrm{human}}N(\boldsymbol{x},t)}D^{(0)}_{\mathrm{eff}}(\boldsymbol{x}) \tag{9}$$

$$\simeq \{1 + \varepsilon_{\mathrm{vol}}N(\boldsymbol{x},t)\}D^{(0)}_{\mathrm{eff}}(\boldsymbol{x}), \tag{10}$$

where Eq. (10) corresponds to the first-order approximation of Eq. (9) and becomes valid for sufficiently small $\varepsilon_{\mathrm{vol}} := V_{\mathrm{human}}/V$.

The second mechanism is related to convective flow around a human body. Srebric, *et al.* [22] reported that the velocity- and length-scales of the convective flow around a human body are 0.1 m/s and 0.6 m. The small-scale convective flow locally perturbs the velocity field $\boldsymbol{u}$ inside the coarse-graining domain $\Omega \times \mathcal{I}$. It has been reported in [28] that the local perturbation induces *phase transition* of the effective diffusion phenomenon; namely, a mobile occupant discontinuously modulates the coefficient $D^{(0)}_{\mathrm{eff}}$ around itself. In this paper, for simplicity of the current modeling, we represent the effect of perturbation as the first-order modulation D_{conv} of $D^{(0)}_{\mathrm{eff}}$:

$$D_{\mathrm{conv}}(\boldsymbol{x},t) := \{1 + \varepsilon_{\mathrm{conv}}N(\boldsymbol{x},t)\}D^{(0)}_{\mathrm{eff}}(\boldsymbol{x}), \tag{11}$$

where $\varepsilon_{\mathrm{conv}}$ is the parameter to quantify the perturbation. Eq. (11) is valid when the kinetic energy of convective flow is smaller than that of nominal flow induced by the air outlets.

Thus, by multiplying the coefficient terms in Eqs. (10) and (11) and ignoring the second-order term of $\varepsilon_{\mathrm{vol}}$ and $\varepsilon_{\mathrm{conv}}$, the following definition of D_{eff} is derived:

$$D_{\mathrm{eff}}(\boldsymbol{x},t) = D^{(0)}_{\mathrm{eff}}(\boldsymbol{x})\left\{1 + \varepsilon N(\boldsymbol{x},t)\right\}, \tag{12}$$

where $\varepsilon := \varepsilon_{\mathrm{vol}} + \varepsilon_{\mathrm{conv}}$ is the control parameter of human effects. The position-dependent function $D^{(0)}_{\mathrm{eff}}(\boldsymbol{x})$ is the effective diffusion coefficient for no human occupancy, i.e. $N(\boldsymbol{x},t) = 0$ for all $\boldsymbol{x}$ and t, and determined with both structural and air characteristics of the target space: see App. B and Sec. IV B. It should be noted that the modulation idea is effective even if the condition (4) does not hold (see App. A).

IV. NUMERICAL IMPLEMENTATION

This section provides numerical implementation of the proposed mathematical modeling in Sec. III to the commercial office space in Sec. II: preliminary investigations of the office space (Sec. IV A); simulation methods (Sec. IV B); discretized formulations of the heat source term P (Sec. IV C); and processing of human occupancy data (Sec. IV D) for the incorporation.

A. Preliminary investigations of modeling target

First of all, we preliminary investigate the air flow and heat transfer in the target space in terms of characteristic numbers and geometry. From the discussion in Sec. III A, the current modeling is conducted to the two-dimensional domain with 40 m (south-to-north) × 10 m (west-to-east). Below, as familiar in fluid mechanics, we decompose the air velocity $\boldsymbol{u}(\boldsymbol{r},t)$ into the time-invariant component $\boldsymbol{u}_0(\boldsymbol{r})$ and the time-varying one $\tilde{\boldsymbol{u}}(\boldsymbol{r},t)$: see e.g. [20].

First, we discuss the relative importance of advection and diffusion in thermal transport with the Péclet number *Pe*. In this paper, the thermal diffusion coefficient D of air is set at $2.25 \times 10^{-5}\,\mathrm{m}^2/\mathrm{s}$ [29], the length-scale L_0 of the averaged flow $\boldsymbol{u}_0$ is set at 1.8 m based on the distance between outlet ducts of HVAC units, and the velocity-scale U_0 of $\boldsymbol{u}_0$ is set at 1.6 m/s from the setting of HVAC-outlet volume. The Péclet number for $\boldsymbol{u}_0$ is calculated as $Pe := L_0U_0/D = 1.3 \times 10^5$. Therefore, the thermal transport by $\boldsymbol{u}_0$ is mainly governed by advection in the target space.

Second, we discuss the flow's state in the target space with the Reynolds number *Re*. For the kinematic viscosity $\nu = 1.4 \times 10^{-5}\,\mathrm{m}^2/\mathrm{s}$ [29], the Reynolds number Re is at least $L_0U_0/\nu = 2.1 \times 10^5$, implying that flow is turbulent. This is relevant in the target space because many outlet ducts of HVAC exist on the ceiling and cause the air flow to be well mixed. For the fully-developed turbulent state $\tilde{\boldsymbol{u}}(\boldsymbol{r},t)$, it is well-known in [20] that a wavenumber component $\tilde{\boldsymbol{u}}_{\boldsymbol{k}}(t)$ with a wavenumber vector $\boldsymbol{k} \in \mathbb{R}^3$ vanishes in its lifespan $\tau_{\boldsymbol{k}}$ [20]. The maximum value of $\tau_{\boldsymbol{k}}$ is calculated as $L_0/U_0 = 1.1\,\mathrm{s}$. Thus, almost all the components of $\tilde{\boldsymbol{u}}$ are averaged to be zero in the target time-interval (1 s) for the simulation (see Sec. IV B). This is a quantitative evidence that the time-average in Eq. (4) is approximately zero, and $D^{(0)}_{\mathrm{eff}}$ is time-invariant.

Third, the symmetric and homogeneous arrangement of outlet ducts in Fig. 1(c) suggests that the outlet air exhibits both spatially-periodic structure of $\boldsymbol{u}_0$ and homogeneous turbulence of $\tilde{\boldsymbol{u}}$. These preliminary investigations show that the in-room thermal transport is represented as an *isotropic* diffusion phenomenon with the effective diffusion coefficient D_{eff} which we explained in Sec. III A.

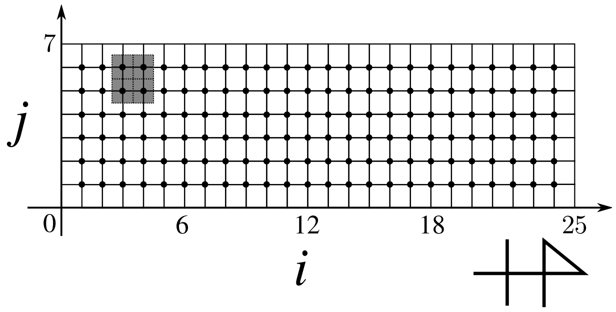

FIG. 2. Spatial coordinates $[i, j]$ fixed at the centers of the detection areas as shown by the shaded domains. The circle symbols denote the inside nodes $[i, j] \in A^{\circ}$.

Finally, we check the time constants of the thermal and fluid effects quantitatively. We set the heat transfer coefficient h_{c} from a human body at $5.0\,\mathrm{W/m^2K}$ [21] and the thickness D_{b} of boundary layer around a human body at $0.11\,\mathrm{m}$ [30]. Also, by setting $\rho = 1.006 \times 10^3\,\mathrm{J/kgK}$ and $c_{\mathrm{p}} = 1.165\,\mathrm{kg/m^3}$, the time constant τ_{t} of heat transfer in the boundary layer, namely the thermal effect, is calculated as $\tau_{\mathrm{t}} = \rho c_{\mathrm{p}} D_{\mathrm{b}}/h_{\mathrm{c}} = 26\,\mathrm{s}$. On the other hand, by setting the walking speed U_{w} of a human occupant at $1\,\mathrm{m/s}$ [26] and the target length-scale L at $1.8\,\mathrm{m}$ (see Sec. IV B), the time constant τ_{f} of the fluid effect is calculated at $L/U_{\mathrm{w}} = 1.8\,\mathrm{s}$. Therefore, it is clear that the thermal effect is slower than the fluid effect in the target space, which we mentioned in the last paragraph of Sec. III A. In addition, the small time constant $\tau_{\mathrm{f}} = 1.8\,\mathrm{s}$ implies that the fluid effect of human occupancy is not fully modeled by the standard homogenization in the target interval of 1 s. Note that as mentioned in Sec. I, the fluid effect requires a completely different CFD project by the time-interval, and thus CFD is unable to predict the effect.

B. Setting for numerical simulations of diffusion equation

This subsection describes a setting for numerical simulations used in this paper: discretization of the diffusion equation (5), assimilation of measured data, and identification of parameters and boundary conditions of the equation.

All numerical simulations of Eq. (5) were performed with the forward-time centered-space method. The discretization step in space was homogeneously set at $\Delta x = \Delta y = 1.8\,\mathrm{m}$, and the spatial coordinates $[i, j]$ were fixed at the centers of detection areas with human sensors as shown in Fig. 2. Here, let us define the following two subsets A° and ∂A to explicitly distinguish the inside and boundary nodes:

$$\begin{aligned} A^{\circ} :=& \{[i,j] : i \in \{1,\dots,24\}, j \in \{1,\dots,6\}\}, \qquad (13)\\ \partial A :=& \{[i,j] : i \in \{1,\dots,24\}, j \in \{0,7\}\} \\ & \cup \{[i,j] : i \in \{0,25\}, j \in \{1,\dots,6\}\}. \qquad (14) \end{aligned}$$

The circle symbols shown in Fig. 2 denote the inside nodes $[i, j] \in A^{\circ}$. The height z was fixed at $2.8\,\mathrm{m}$ for comparison with temperature data measured by task-units on the ceiling. Also, the time period for simulations was set at 9:00 to 18:00 because the operational conditions of HVAC units were fixed during this period. The discretization step in time was set at $\Delta t = 0.1\,\mathrm{s}$. Here, let us introduce a positive integer k_{cal} to represent the discrete time instant equally divided by the step Δt:

$$t = t_0 + k_{\mathrm{cal}} \Delta t, \qquad (15)$$

where t_0 stands for initial time. In this paper we compute the temperature distribution under $\Delta t = 0.1\,\mathrm{s}$ and sample it uniformly in time by 1 s because of the simple handling of data. The sampled temperature distribution is denoted as $T[i, j, k]$ (without use of superscript of H), where $k = 1, \dots, 32400$ represents the discrete time instant equi-sampled by 1 s, and the number of time instants corresponds to 9 hours for simulations.

In the current modeling, we incorporate measured data into the diffusion equation model, namely, conduct data assimilation. For the target office space, the data on human occupancy and on temperature of the atrium and outdoor were measured under sampling of non-uniform periods larger than the simulation step $\Delta t = 0.1\,\mathrm{s}$. The standard zero-order hold was used to construct sampled data by 0.1 s from original ones, and thereby the measured data were incorporated into the diffusion equation (5).

The diffusion equation (5) has many parameters determining the model performance. Below, we identify values of the parameters except for those in $P(\boldsymbol{x}, t)$, which are identified in Sec. IV C. The constants ρ and c_{p} are set at $1.006 \times 10^3\,\mathrm{J/kgK}$ and $1.165\,\mathrm{kg/m^3}$. For the effective coefficient, if we do not consider its position-dependence, its value is nominally calculated as $1.2\,\mathrm{m^2/s}$: see App. B. However, since the outlet ducts in the target office space are not placed in a homogeneous manner, it is necessary to consider the position dependence of the effective coefficient. At the inside nodes $i = 1$ or $j = 1, 6$ faced to the walls or atrium, there is no outlet duct on the side of the walls or atrium. Thus, the thermal transport is induced only by air outlet from the in-room ducts, and the number of ducts governing the thermal transport is half of that for any internal node. For these reasons, we regard the amount of transported heat flux at the nodes as a half of the nominal one:

$$D_{\mathrm{eff}}^{(0)}[i,j] = \begin{cases} 0.6\,\mathrm{m^2/s} & (i = 1 \text{ or } j = 1, 6), \\ 1.2\,\mathrm{m^2/s} & (\text{otherwise}). \end{cases} \qquad (16)$$

Moreover, we fix the control parameter ε at 1.0 in order to simply perform simulations. The parameter indeed controls the fluid effect on in-room temperature distribution

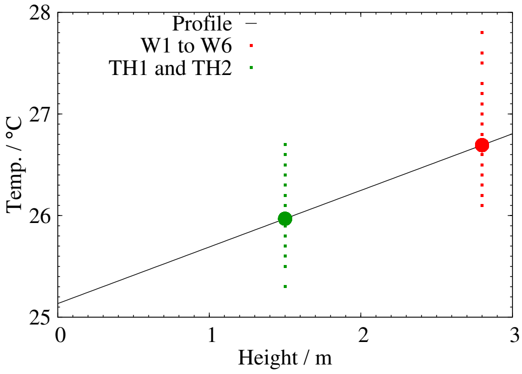

FIG. 3. Measured temperature profile in the height direction of the target office on August 2, 2014 (Saturday: non-working day). The large red and green points indicate the averaged values of temperature data in terms of length, width, and time.

(see [17] in detail). To determine ε in a relevant manner poses a challenging subject and remains to be solved in literature. Note that in [28] the authors investigate a time-periodic perturbation of incompressible fluid flows, related to the advective contribution $\varepsilon_{\rm conv}$ in ε.

Next, we identify the coefficient c of the temperature profile (3) in height z. For this, let us compute the spatio-temporal average of Eq. (2) in the horizontal (namely, length x and width y) direction and time t:

$$\frac{1}{|A||I|}\int_{A\times I} T(x,y,z,t)\mathrm{d}x\mathrm{d}y\mathrm{d}t = \frac{1}{|A||I|}\int_{A\times I} T^{\rm H}(x,y,t)\mathrm{d}x\mathrm{d}y\mathrm{d}t + c\left(z-\frac{h}{2}\right), \quad (17)$$

where $|A|$ stands for the total area of A and I for a finite time interval with length $|I|$. The height z appears linearly on the right-hand side of Eq. (17), and thus it is possible to identify the slope c by using temperature data measured at different heights. Since it is not feasible to densely deploy temperature sensors in the practically used office space, we use the temperature data measured at two heights. Figure 3 shows measured temperature profile in the height direction on August 2, 2014 (Sat.). The red points stand for the temperature data measured by W1 to W6 (height 2.8 m) and the green ones for TH1 and TH2 (height 1.5 m). The large red point in the figure represents the value of spatio-temporal average of data denoted by all the small red points and the large green point for the average value of the green points. The *solid* line corresponds to the linear function (17) identified by the data on the above day, where c is calculated at 0.557 °C/m. Since on this non-working day there were few people in the target space, the measured data are expected to capture the nominal profile of air temperature in the height direction. Thus, we set the coefficient c at 0.557 °C/m in the following simulation.

Finally, we make the boundary conditions of Eq. (5) for numerical simulations. The boundary conditions at $[i,j]\in\partial A$ were determined by using the data on temperature measured at the outside of the target space. For the boundary on a wall, the Neumann-type boundary condition was adopted. In this condition, the convective heat input $P_{\rm conv}$ from the wall was modeled in Sec. IV C. For no wall on the boundary, the Dirichlet-type boundary condition was adopted. The boundary conditions and measurement data used there are summarized in Tab. II, where ∂A is decomposed into the seven subsets.

C. Discretized formulations of heat source P

The heat source $P(\boldsymbol{x},t)$ is decomposed into the six terms as in Eq. (6). In this subsection, we model the heat source terms as discretized forms that are directly implemented for numerical simulations.

1. $P_{\rm HVAC}$ *and* $P_{\rm solar}$

In this paper, we formulate the sum of inputs $P_{\rm HVAC}+P_{\rm solar}$ and do not consider the input $P_{\rm solar}$ solely. The HVAC in the target space manages to suppress the temperature change due to oscillatory solar radiation. The suppression is hard to model in the target space because no information on the HVAC management is available. See App. D for sole formulation of $P_{\rm solar}$ based on information of solar radiation. Here, the heat input $P_{\rm HVAC}+P_{\rm solar}$ can take a non-zero value at every node with outlet duct; otherwise, it is identically 0 W/m^3. Based on the formula known as *bulk convection* [1], $P_{\rm HVAC}+P_{\rm solar}$ is given as follows:

$$P_{\rm HVAC}[i,j,k]+P_{\rm solar}[i,j,k] = \frac{\rho c_{\rm p} V[i,j,k](T_{\rm HVAC}[i,j,k]-T[i,j,k])}{h\Delta x^2 N_{\rm duct}[i,j]}, \quad (18)$$

where $V[i,j,k]$ stands for the outlet volume per unit time at node $[i,j]$ and time k, $T_{\rm HVAC}[i,j,k]$ for the air temperature at the outlet, $h=2.8$ m for the height of the target space, and $N_{\rm duct}[i,j]$ for the number of ducts connected with the HVAC unit that supplies air at the node $[i,j]$ in Fig. 1(c). Assuming that the outlet volume V does not change in time, we use the nominal values of outlet volume shown in Tab. I for $V[i,j]$. Also, the measured data on outlet temperature of ambient-units are used as $T_{\rm HVAC}$. However, the outlet temperature of task-units is not measured. For simplicity of the current modeling, we set the temperature $T_{\rm HVAC}$ of task-units to be constant shown in Tab. III. These values—20 °C and 21 °C—were determined with the data on outlet temperature of ambient-units on July 31 and August 2, 2014. Note that the cooling input is partly canceled by $P_{\rm conv}$

TABLE II. Settings of boundary conditions at $[i, j] \in \partial A$. Types of the boundary conditions, data used for the conditions, and overall heat transfer coefficient U of each boundary wall are shown.

Boundary	Node $[i, j]$	Type	Used data	$U\,[\mathrm{W/m^2K}]$
∂A_{E1}	$\{1, \ldots, 4, 9, \ldots, 12, 17, \ldots, 20\} \times \{0\}$	Neumann	Outdoor	1.6
∂A_{E2}	$\{5, 6, 13, \ldots, 16, 21, 22\} \times \{0\}$	Neumann	Outdoor	1.0
∂A_{E3}	$\{7, 8, 23, 24\} \times \{0\}$	Neumann	Booth	2.0
∂A_{S}	$\{0\} \times \{1 \ldots 6\}$	Neumann	Meeting room	2.0
∂A_{N}	$\{25\} \times \{1 \ldots 6\}$	Dirichlet	Office	—
∂A_{W1}	$\{1 \ldots 8\} \times \{7\}$	Neumann	—	0.0
∂A_{W2}	$\{9 \ldots 24\} \times \{7\}$	Dirichlet	Atrium	—

TABLE III. Settings of temperature parameter T_{HVAC}.

	July 31, 2014	August 2, 2014
Task-unit	20 °C	21 °C
Ambient-unit	Measured data	Measured data

(see App. C), and thus the simulated and measured in-room temperatures become higher than the outlet one (see Figs. 3, 7, and 8).

2. P_{conv}

We model the convective heat transfer P_{conv} as the Neumann-type boundary conditions of Eq. (5) and do not hence explicitly include this term in Eq. (6). In the boundary conditions, the temperature $T[i_{\mathrm{b}}, j_{\mathrm{b}}, k]$ at boundary node $[i_{\mathrm{b}}, j_{\mathrm{b}}] \in \partial A$ and time k is set as follows:

$$\frac{T[i_{\mathrm{b}}, j_{\mathrm{b}}, k] - T[i, j, k]}{\Delta x} = K_{\mathrm{conv}}[i_{\mathrm{b}}, j_{\mathrm{b}}, k](T_{\mathrm{ext}}[k] - T[i, j, k]), \quad (19)$$

where $[i, j] \in A^{\circ}$ stands for the node next to $[i_{\mathrm{b}}, j_{\mathrm{b}}]$. The parameter $K_{\mathrm{conv}}[i_{\mathrm{b}}, j_{\mathrm{b}}, k]$ represents the coefficient to describe the effect of convective heat flow and $T_{\mathrm{ext}}[k]$ the measured data of external temperature. The data were sampled in a meeting room, booth, and outdoor. Eq. (19) expresses the heat flow from the outside through walls, namely *overall heat transfer* [1], for the assumption of uniform distribution of in-wall temperature. The convection coefficient $K_{\mathrm{conv}}[i_{\mathrm{b}}, j_{\mathrm{b}}, k]$ is estimated as follows:

$$K_{\mathrm{conv}}[i_{\mathrm{b}}, j_{\mathrm{b}}, k] = \frac{U[i_{\mathrm{b}}, j_{\mathrm{b}}]}{\rho c_{\mathrm{p}} D_{\mathrm{eff}}[i, j, k]}, \quad (20)$$

where $U[i_{\mathrm{b}}, j_{\mathrm{b}}]$ is the overall heat transfer coefficient shown in Tab. II. The estimation of K_{conv} is given in App. E.

3. P_{rad}

Thermal radiation appears through the eastern glass windows faced to the outdoor. In this paper, we model the radiation heat transfer by linear thermal resistance [1]. More specifically, we make the following three assumptions on the modeling of thermal radiation:

(A1) Temperature of glass wall is the same as outdoor temperature;

(A2) Transient change in temperature on surfaces of indoor walls is negligible;

(A3) Temperature on surfaces of indoor walls and view factors between the walls are spatially uniform.

The first assumption is reasonable because glass wall has a high thermal conductivity. The second one is also reasonable if the outdoor temperature changes slowly. The third one is used in the existing approach similar to *Mean Radiant Temperature (MRT) method* [1]. Thus, by using series connection of thermal resistances, the following formula of P_{rad} is derived:

$$P_{\mathrm{rad}}[i, j, k] = K_{\mathrm{rad}}[i, j](T_{\mathrm{out}}[k] - T[i, j, k]), \quad (21)$$

where $T_{\mathrm{out}}[k]$ stands for the measured data on outdoor temperature. The parameter K_{rad} at internal node $[i, j] \in A^{\circ}$ is determined with thermal radiation and convection resistances in the following manner:

$$K_{\mathrm{rad}}[i, j] = \begin{cases} \dfrac{2/h}{R_{\mathrm{ceil}} + R_{\mathrm{conv}}} + \dfrac{1/\Delta x}{R_{\mathrm{west}} + R_{\mathrm{conv}}}, \\ \qquad \text{if } i \in \{2, \ldots, 8\},\ j = 6, \\ \dfrac{2/h}{R_{\mathrm{ceil}} + R_{\mathrm{conv}}} + \dfrac{1/\Delta x}{R_{\mathrm{south}} + R_{\mathrm{conv}}}, \\ \qquad \text{else if } i = 1,\ j \in \{1, \ldots, 5\}, \\ \dfrac{2/h}{R_{\mathrm{ceil}} + R_{\mathrm{conv}}} + \dfrac{1/\Delta x}{R_{\mathrm{south}} + R_{\mathrm{conv}}} \\ \quad + \dfrac{1/\Delta x}{R_{\mathrm{west}} + R_{\mathrm{conv}}}, \quad \text{else if } i = 1,\ j = 6, \\ \dfrac{2/h}{R_{\mathrm{ceil}} + R_{\mathrm{conv}}}, \quad \text{else.} \end{cases} \quad (22)$$

As shown in Fig. 4, R_{ceil}, R_{west}, and R_{south} stand for the

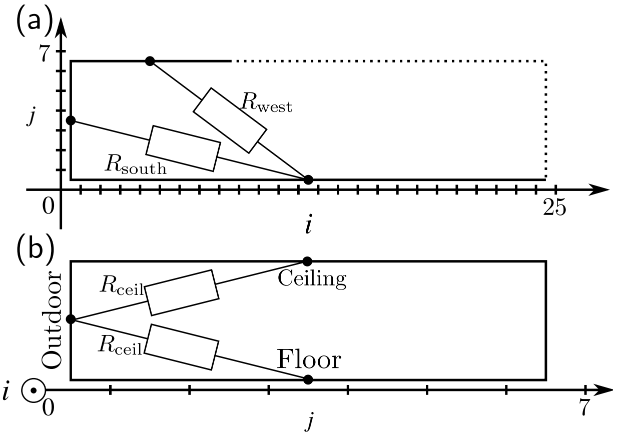

FIG. 4. Thermal resistances of radiation from the eastern glass-wall (a) to the western and southern walls and (b) to the ceiling and floor.

TABLE IV. Values of thermal resistances R_{ceil}, R_{west}, R_{south}, and R_{conv} [m^{2}K/W].

R_{ceil}	R_{west}	R_{south}	R_{conv}
0.143	0.155	0.185	0.500

thermal resistances of long-wave radiation from the eastern glass-wall to the ceiling (or floor), western wall, and southern wall, respectively. These resistances are calculated as the *radiation coefficient* in the MRT method [1]. Also, R_{conv} stands for the thermal resistance of convection from each surface. In this paper, R_{conv} is regarded as the same value for every wall. Table IV shows the values of thermal resistances used in the rest of this paper.

4. P_{eqp}

For simplicity of the current modeling, we assume that the heat input P_{eqp} from office equipment is spatially uniform in the target space. By referring to practical values of power consumption by office equipment [1], P_{eqp} is set as follows:

$$P_{\mathrm{eqp}} = 7.2\,\mathrm{W/m^3}. \tag{23}$$

5. P_{human}

The heat input P_{human} from human occupants is derived as Eq. (7). By regarding a single human occupant as a heat source of 75 W [1], the coefficient P_0 in Eq. (7) is defined as follows:

$$P_0 = \frac{75\,\mathrm{W}}{h\Delta x^2}, \tag{24}$$

where the denominator corresponds to the fixed volume of one node in the current space-discretization.

D. Processing of human sensor data for incorporation

The main idea in the current paper is to incorporate human occupancy data into the diffusion equation model. In this subsection, we consider how to process the data for the incorporation. As mentioned in Sec. III B, the human occupancy influences in-room thermal dynamics in a multiscale manner. For effectively modeling the influence, we extract a dominant spatio-temporal mode embedded in the data and incorporate it into the equation via the two parameters P_{human} and D_{eff}. Below, let us represent measured data on human occupancy with a sequence of vectors $\boldsymbol{N}[k]$ labeled by discrete time $k = 0, 1, \dots$ that corresponds to a spatially discretized form of $N(\boldsymbol{x}, t)$. The dimension of $\boldsymbol{N}[k]$ is equal to the number of nodes $[i, j]$.

There are many existing methods for extracting a spatio-temporal mode from data. In this paper, we use the POD (Proper Orthonormal Decomposition) [24] for the extraction from one-day data on human occupancy. POD provides the most efficient way of capturing a mode oscillating with (possibly) multiple frequencies in the energy (precisely L_2) sense and is hence suitable for the current thermal modeling. Consider finite measurement data on human occupancy, $\{\boldsymbol{N}_0[k] \in \mathbb{R}^{n_{\mathrm{g}}}\}$ ($k = 0, \dots, n_{\mathrm{s}} - 1$), where n_{g} is the number of all grid nodes and n_{s} is the number of samples: $n_{\mathrm{g}} = 144$ and $n_{\mathrm{s}} = 86400$ for the target office space and available data. The data are represented by

$$\boldsymbol{N}_0[k] = \sum_{m=1}^{n_{\mathrm{g}}} a_m[k] \boldsymbol{V}_m. \tag{25}$$

The time-invariant basis vectors $\{\boldsymbol{V}_m \in \mathbb{R}^{n_g}\}$ ($m = 1, \dots, n_{\mathrm{g}}$) are required to be orthonormal and closest in energy norm to the data, called the POD modes. The time-varying coefficients a_m ($m = 1, \dots, n_{\mathrm{g}}$) hold the following correlation property: $\langle a_m a_n \rangle = \langle a_m^2 \rangle$ (if $m = n$) or 0 (else), where $\langle \cdot \rangle$ represents the time-average of scalar-valued signal. The notation $\langle a_m^2 \rangle$ implies the energy contained in the m-th POD mode. POD modes are generally ordered in the contained energy by $\langle a_m^2 \rangle \geq \langle a_{m+1}^2 \rangle$.

Figure 5(a) shows the proportion of $\langle a_m^2 \rangle$ to all the energy in the first ten POD modes obtained for the human sensor data on July 31, 2014. In this figure, the first POD mode has the largest percentage (about 40 %) of all the energy. This clearly shows that the first POD mode is dominant in the spatio-temporal dynamics of human occupancy. Here, the residual energy is widely dispersed among the higher-order modes $a_m[k]\boldsymbol{V}_m$ ($m \geq 2$), implying that any linear combination of multiple higher-order modes fails to provide a good approximation of the dynamics. Figures 5(b) and 5(c) show the spatial shape

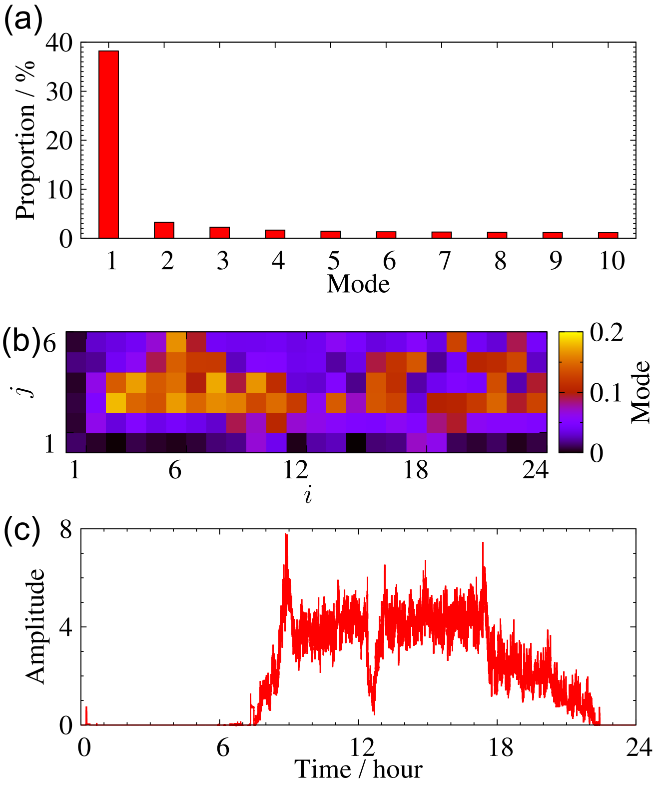

FIG. 5. Modal information extracted by POD from human sensor data on July 31, 2014: (a) proportion of energy $\langle a_m^2 \rangle$ of the m-th POD mode; (b) spatial shape of the first POD mode $\boldsymbol{V}_1$; and (c) time-varying coefficient a_1.

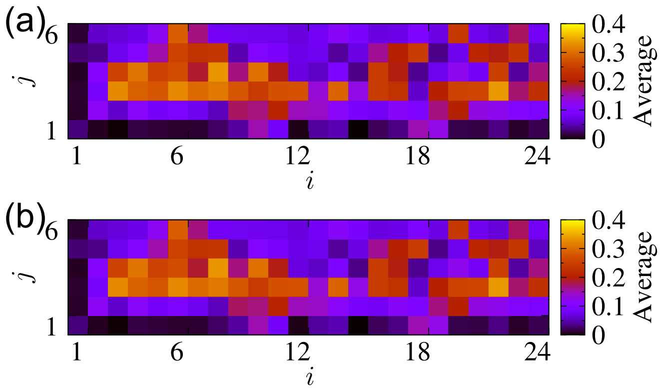

FIG. 6. Spatial shapes of the time-averages of human occupancy on July 31, 2014: (a) $\langle \boldsymbol{N}_0 \rangle$ of $\boldsymbol{N}_0[k]$ and (b) $\langle a_1 \rangle \boldsymbol{V}_1$ of $a_1[k]\boldsymbol{V}_1$.

TABLE V. Incorporation of human occupancy data into the diffusion equation (5). The function of human occupancy is represented by $N(\boldsymbol{x}, t)$, and its discretized form for data processing and simulations is denoted as $\boldsymbol{N}[k]$. For the original measured data $\boldsymbol{N}_0[k]$, the product of time-varying coefficient and spatial shape of the first POD mode is denoted as $a_1[k]\boldsymbol{V}_1$. The constant P_0 is the heat value of a single human occupant in Eq. (24), $D_{\text{eff}}^{(0)}(\boldsymbol{x})$ the stationary effective diffusion coefficient in Eq. (16), and ε the control parameter for the fluid effect in Eq. (12).

Case	$\boldsymbol{N}[k]$	$P_{\text{human}}(\boldsymbol{x}, t)$	$D_{\text{eff}}(\boldsymbol{x}, t)$
0	$\boldsymbol{0}$	0	$D_{\text{eff}}^{(0)}(\boldsymbol{x})$
1-a	$\boldsymbol{N}_0[k]$	$P_0 N(\boldsymbol{x}, t)$	$D_{\text{eff}}^{(0)}(\boldsymbol{x})$
1-b	$a_1[k]\boldsymbol{V}_1$	$P_0 N(\boldsymbol{x}, t)$	$D_{\text{eff}}^{(0)}(\boldsymbol{x})$
2-a	$\boldsymbol{N}_0[k]$	0	$D_{\text{eff}}^{(0)}(\boldsymbol{x})\,\{1 + \varepsilon N(\boldsymbol{x}, t)\}$
2-b	$a_1[k]\boldsymbol{V}_1$	0	$D_{\text{eff}}^{(0)}(\boldsymbol{x})\,\{1 + \varepsilon N(\boldsymbol{x}, t)\}$
3	$\boldsymbol{N}_0[k]$	$P_0 N(\boldsymbol{x}, t)$	$D_{\text{eff}}^{(0)}(\boldsymbol{x})\,\{1 + \varepsilon N(\boldsymbol{x}, t)\}$

of the first POD mode $\boldsymbol{V}_1$ and its corresponding time-varying coefficient a_1. The spatial shape in Fig. 5(b) almost coincides with the spatial distribution of sitting workers observed in the target office space. This is confirmed with the fact that the components of $\boldsymbol{V}_1$ take smaller values along the edges (namely, nodes labeled by $i = 1$ or $j = 1$) corresponding to the aisle of the target office.

Here, let us compare the POD mode with the original data. For the current comparison, we calculate time-averages of the original data $\boldsymbol{N}_0[k]$ and of the sequential data $a_1[k]\boldsymbol{V}_1$ with respect to the first POD mode. The time-averaging technique is used in [31] for comparing long-term behaviors of dynamical system models. Figure 6 shows the spatial shapes of the time-averages $\langle \boldsymbol{N}_0 \rangle$ and $\langle a_1 \rangle \boldsymbol{V}_1$. The similarity of the spatial shapes implies that the first POD mode captures well the long-term trend in the dynamics of human occupancy, in other words, the time-averaged or bias component—the thermal effect discussed later. Also, as shown in Fig. 5(c), the time-varying coefficient $a_1[k]$ clearly contains multiple frequencies, and thus the first POD mode is expected to capture a short-term variation in the occupancy dynamics causing the fluid effect. Based on these observations, we will perform numerical simulations of the target office space with $\boldsymbol{N}_0[k]$ and $a_1[k]\boldsymbol{V}_1$ as discretized forms of $N(\boldsymbol{x}, t)$. The simple description based on the single dominant mode $a_1[k]\boldsymbol{V}_1$ provides an efficient way of saving computational resources; for example, memory and storage devices used for the human occupancy data.

Finally, based on the above data processing and analysis, we describe a concrete scheme for incorporating human occupancy data in the diffusion equation. The concrete scheme used in numerical simulations of the next section is summarized in Tab. V. In Case:0, no data on human occupancy are utilized and the simulation results are compared with the other cases. In Case:1-a and Case:1-b, only the heat source P_{human} is incorporated. Thus, the thermal effect due to human occupancy is investigated in the two cases. Also, the effective diffusion coefficient D_{eff} for the fluid effect is incorporated in Case:2-a and Case:2-b. Finally, both the heat source and effective diffusion coefficient are incorporated in Case:3

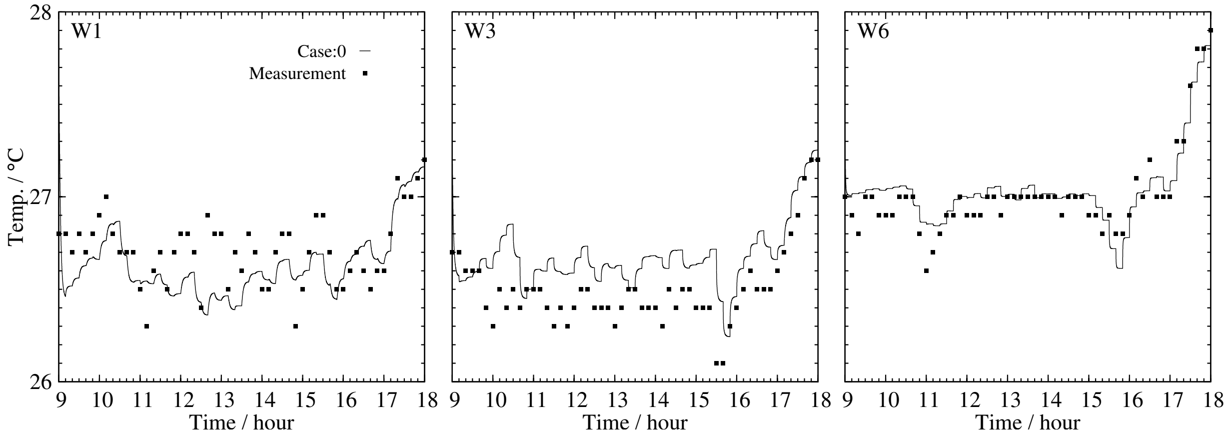

FIG. 7. Simulation results of in-room temperature of the target office on August 2, 2014 (Sat.; non-working day) in Case:0.

towards the goal of the current modeling.

V. NUMERICAL SIMULATIONS AND DISCUSSION

A. Simulation results

This subsection presents a collection of numerical simulations of in-room temperature for the target office space in Fig. 1. The simulations are conducted by incorporating the diffusion equation model (5) with measured data on human occupancy based on the scheme summarized in Tab. V. First of all, we present simulated time-series for Case:0 on a non-working day, namely, without incorporation of human occupancy data. Then, we show simulation results for both Case:1 and Case:2 on a working day and point out the multiscale influence of human occupancy on in-room temperature in time. Spatial distributions of the simulation results are also shown so that the multiscale features are pointed out in space. From the fact that the temperature was measured at the air ducts, namely on the ceiling, all the simulated temperature includes the steady vertical component $T^{\mathrm{V}}(h)$.

Figure 7 shows a simulation result of temperature at the locations of task-units W1, W3, and W6 on August 2, 2014 (Sat.). The result was obtained for Case:0 in Tab. V, namely, without incorporation of human occupancy data. This day was a non-working day for this building and hence suitable to verifying the ability of the diffusion equation (5) for nominal thermal dynamics not influenced by human occupancy. Measurement indeed shows that there were very few occupants in the target office space on this day. In Fig. 7, we see that the simulated time-series denoted as *solid* curves exhibit temporal variations close to the measured data. The proposed modeling captures the temporal variation of the nominal thermal dynamics in the target space without any inclusion of air motion. Here, we see at W1 and W3 in Fig. 7 that the time-averaged (bias) components in the measured and simulated data are slightly different. This is partly because the amount of heat input P_{eqp} is position-dependent, namely non-uniform, although the amount is assumed to be uniform in the current modeling of Eq. (23).

Figures 8(a)–(c) show simulation results on July 31, 2014 (Thu.), where human occupancy data are incorporated via the scheme summarized in Tab. V. First of all, we describe how the data incorporation appears in the temperature simulations. In Fig. 8(a), the simulated temperature in Case:1 is higher than Case:0, more precisely, the bias component increases by incorporating the data into the input heat term P_{human}. In Fig. 8(b), the oscillatory amplitude of temperature in Case:2 is larger than Case:0, that is to say, the deviation of temperature from the bias component increases by incorporating the data into the effective diffusion coefficient D_{eff}. In Fig. 8(c), by the incorporation into both P_{human} and D_{eff}, the bias and deviation components become large compared with Case:0. Also, by the data incorporation, the temporal behaviors in Case:1 to Case:3 become close to the measured one. It should be noted that these observations hold in simulations on another day (see the supplemental figures in detail).

Figure 9(a) shows spatial shapes of the simulated temperature distributions at discrete time $k = 15600$ on July 31, 2014 (Thu.). The shapes in Case:1, Case:2, and Case:3 are different from Case:0, implying that the thermal and fluid effects spatially work on the in-room temperature distribution. For detailed investigation of these effects, we calculate the derivative of simulated temperature with respect to that in Case:0, denoted as $\triangle_{n_{\mathrm{c}}}$ for $n_{\mathrm{c}} \in \{1\text{-}a, 1\text{-}b, 2\text{-}a, 2\text{-}b, 3\}$:

$$\triangle_{n_{\mathrm{c}}}[i,j,k] := T_{n_{\mathrm{c}}}[i,j,k] - T_0[i,j,k], \tag{26}$$

where $T_{n_{\mathrm{c}}}$ stands for the simulation result in Case:n_{c} and T_0 for Case:0. Figures 9(b) and (c) show the spatial shapes of T_0 (first row) and $\triangle_{n_{\mathrm{c}}}$ (second to sixth rows) at

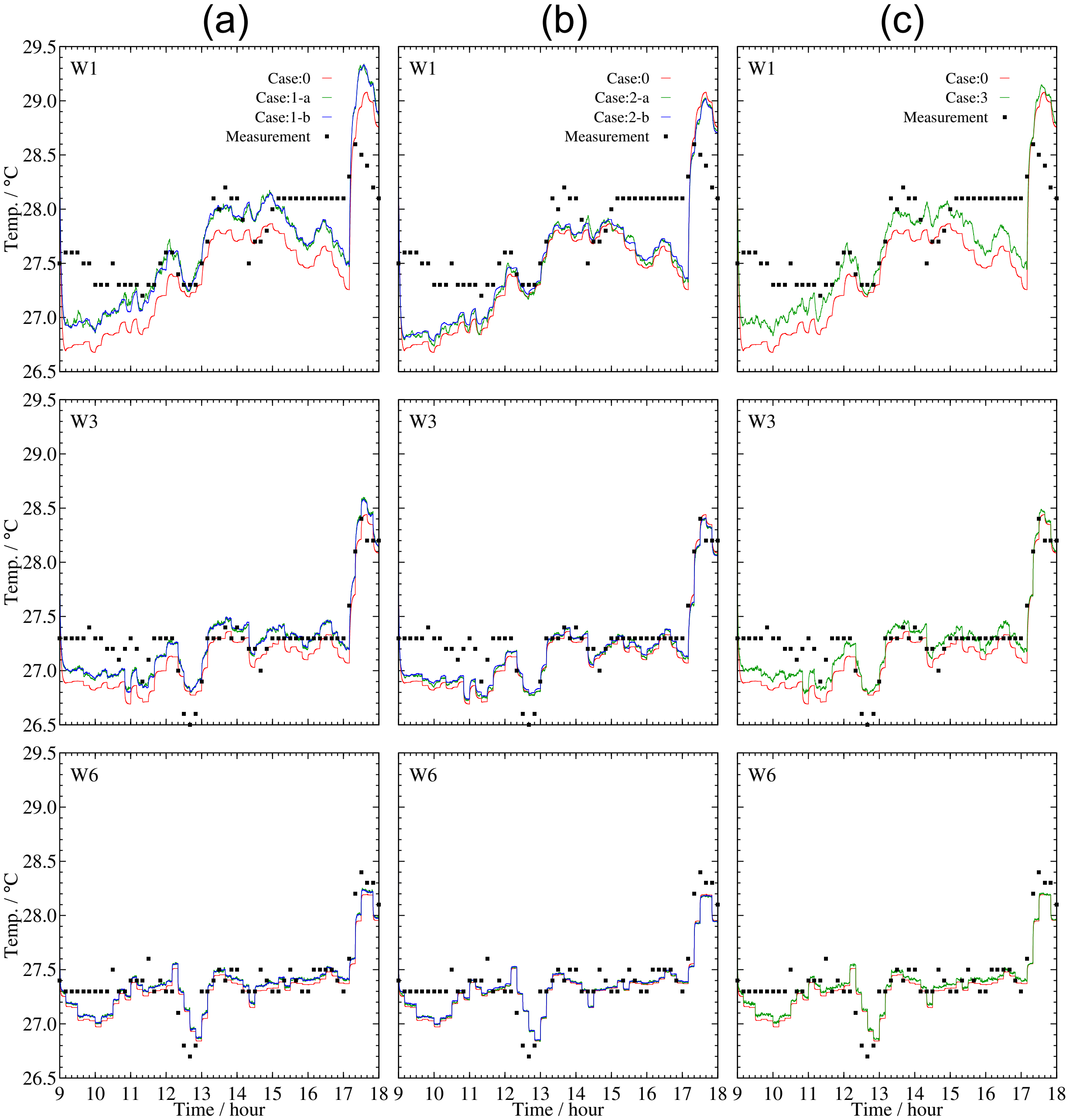

FIG. 8. Simulation results of in-room temperature of the target office on July 31, 2014 (Thu.; working day): (a) Case:0, Case:1-a, and Case:1-b; (b) Case:0, Case:2-a, and Case:2-b; and (c) Case:0 and Case:3.

$k = 15600$ and $k = 15900$, respectively. The derivatives in Case:1 take non-zero values globally, and their spatial shapes do not change from $k = 15600$ to 15900. On the other hand, the derivatives in Case:2 become non-zero in several local domains, and these domains temporally move from the center to the left of the figures: see the domains encompassed by the white lines in Case:2-a (see also the supplemental movie). These observations are consistent in Case:3, and both effects appear in the spatial shapes of temperature. The snapshots of the temperature derivatives show that the thermal and fluid effects, which are modeled via P_{human} and D_{eff}, are globally slow and locally fast effects on the in-room temperature distribution.

Finally, we report the computational efficiency of the modeling. It took about 7.3 s in every case to simulate 9-hour time-series shown in Figs. 7 and 8, where we utilized a general-purpose computer including 4 core CPU driven at 3.40 GHz and 8 MB cache. This clearly shows the potential of the proposed modeling for real-time con-

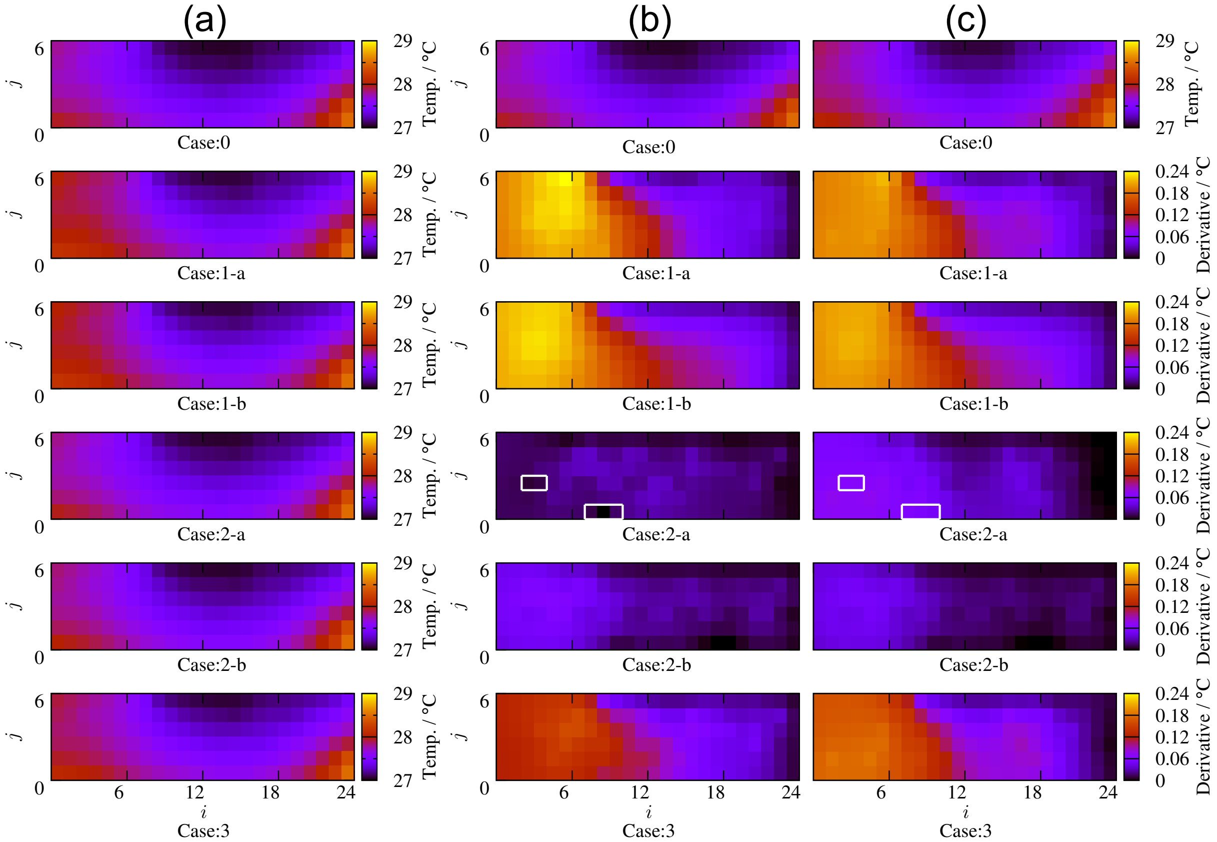

FIG. 9. Spatial shape of simulated temperature distribution and its derivative: (a) simulated distribution at $k = 15600$; (b) simulated distribution in Case:0 and derivative $\triangle_{n\mathrm{c}}$ in the other cases at $k = 15600$; and (c) simulated distribution in Case:0 and derivative $\triangle_{n\mathrm{c}}$ in the other cases at $k = 15900$. In Case:2-a, the derivatives are non-zero especially in the domains encompassed by the white lines, and these domains move in time.

trol of in-room temperature. Such a fast simulation of in-room temperature is not possible with CFD because of its computational burden for the dynamic fluid effect.

B. Quantifying thermal and fluid effects

The snapshots in Fig. 9 provided an evidence that the data-incorporated modeling involved the thermal and fluid effects. Now, we conduct detailed analyses of the simulated temperature distributions in order to quantify how these effects appear in the simulations and how similar the simulated and measured behaviors are.

Figure 10(a) shows the spatial dependence of the time-averages (bias components) $\langle T\rangle[i,j]$ of the simulation results $T[i,j,k]$. In the right domain of the figure (a), the time-averages do not change in all the cases. This is mainly because the heat input from the atrium placed at the right top of each figure is strong and overwhelms (in average) the heat input from human occupants. In contrast, the left domain has no dominant influence by the atrium, and hence the time-averages are dependent on the cases, namely the scheme of data incorporation. Figure 10(b) shows the time-averages $\langle T\rangle$ and $\langle T_{\mathrm{m}}\rangle$ at W1, W3, and W6, where $T_{\mathrm{m}}[i,j,k_{\mathrm{m}}]$ stands for the measured data with time instant $k_{\mathrm{m}} = 1,\ldots,54$. The time-averages $\langle T\rangle$ in Case:1 and Case:3 become higher than Case:0 and approach to that of the measured data. Here, the time-averages $\langle T\rangle$ in Case:0 and Case:2 are almost same. The averaging results quantitatively prove that the data incorporation into P_{human} represents the thermal effect by human occupancy and contributes to the accurate modeling. Also, in Fig. 10(a), the distributions of time-averages of the simulated temperatures in Case:1-a and Case:1-b are quantitatively similar. This implies that the thermal effect by human occupancy is captured well with the POD mode which represents the long-term trend in the dynamics of human occupancy. Thus, it is quantified by using the time-average how human occupancy works on the in-room temperature distribution via the thermal effect.

Next, we consider the deviations of temperature from the time-averages (bias components) discussed in the above paragraph. Figures 11(a) and (b) show the deviations $\tilde{T}[i,j,k]$ and $\tilde{T}_{\mathrm{m}}[i,j,k_{\mathrm{m}}]$ of the simulated and measured temperatures at W1, W3, and W6. The position-

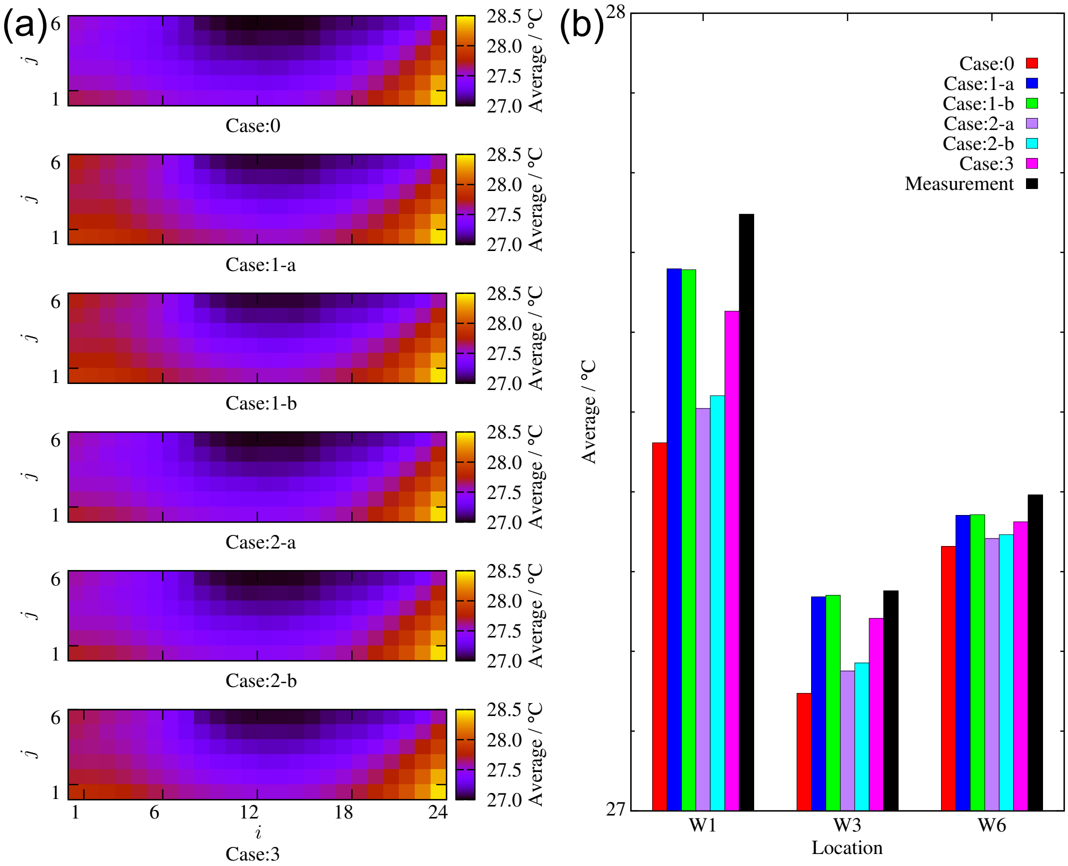

FIG. 10. Time-averages $\langle T\rangle[i,j]$ and $\langle T_{\rm m}\rangle[i,j]$ of the simulated temperatures $T[i,j,k]$ and the measured data $T_{\rm m}[i,j,k]$ on July 31, 2014 (Thu.: working day): (a) spatial dependence of $\langle T\rangle[i,j]$ and (b) values of $\langle T\rangle[i,j]$ and $\langle T_{\rm m}\rangle[i,j]$ at W1, W3, and W6.

dependent deviations $\tilde{T}[i,j,k]$ and $\tilde{T}_{\rm m}[i,j,k_{\rm m}]$ are defined as

$$\tilde{T}[i,j,k] := T[i,j,k] - \langle T\rangle[i,j], \tag{27}$$

$$\tilde{T}_{\rm m}[i,j,k_{\rm m}] := T_{\rm m}[i,j,k_{\rm m}] - \langle T_{\rm m}\rangle[i,j]. \tag{28}$$

The figures (a) and (b) show that the temporal deviations in Case:1 to Case:3 are different from that in Case:0, namely, they change by incorporating the data on human occupancy. In particular, the changes of temporal deviations clearly appear in Case:2 and Case:3 and become similar to that of the measured one: see the enlarged temporal shapes at W1 in Fig. 11(a) and (b). In order to quantify the similarity, in Fig. 11(c) we show the distance $\tilde{d}[i,j]$ between the deviations $\tilde{T}[i,j,k]$ and $\tilde{T}_{\rm m}[i,j,k_{\rm m}]$ at W1, W3, and W6, that is to say, a metric between two different scalar-valued signals. The distance $\tilde{d}[i,j]$ is based on the standard L_2 norm of scalar-valued signal space and defined as follows:

$$\tilde{d}[i,j] := \left\{ \sum_{k_{\rm m}=1}^{54} \left| \tilde{T}[i,j,600k_{\rm m}] - \tilde{T}_{\rm m}[i,j,k_{\rm m}] \right|^2 \times (1\,{\rm s}) \right\}^{1/2}. \tag{29}$$

The values of distance in Case:0 and Case:1 are almost the same for every location. But, the values in Case:2 and Case:3 are smaller than Case:0. The distance results quantitatively prove that the data incorporation into $D_{\rm eff}$ models the fluid effect by human occupancy. Also, the distance in Case:2-b using the dominant POD mode is smaller than Case:2-a using the original data set. This is possibly due to a sub-side effect of the POD-based data processing. Any sensor data contain inevitable measurement error: in this work, it corresponds to a component not related to the real human movement. Since the POD captures a dominant trend of the human occupancy movement in energy norm, the energy-less error component is captured in higher-order modes and does not affect the incorporation in Case:2-b. Thus, the substantial component to reproduce the fluid effect is extracted by the POD-based processing and results in a better consistency of the simulated and measured data on temperature. Hence, by using the distance defined in Eq. (29), it is quantified how the fluid effect is modeled for accurate modeling of in-room temperature.

Finally, we comment on the combined thermal and fluid effects on in-room temperature distribution observed in Case:3. Figures 10 and 11 show that the time-averages $\langle T\rangle$ and deviations $\tilde{T}$ in Case:3 are different from Case:0. These prove that the data incorporation

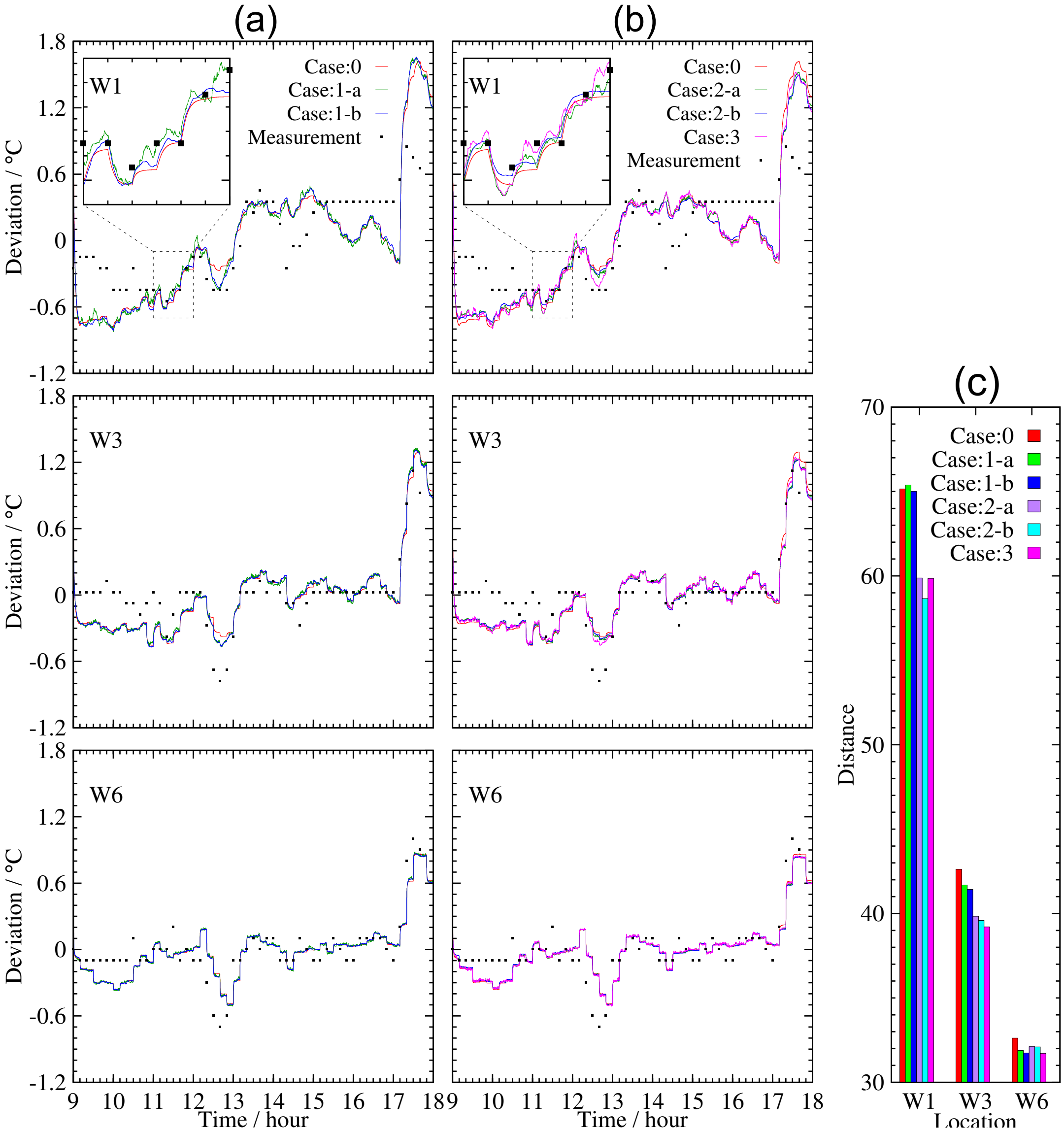

FIG. 11. Deviations $\tilde{T}[i,j,k]$ and $\tilde{T}_\mathrm{m}[i,j,k_\mathrm{m}]$ of the simulated temperatures $T[i,j,k]$ and the measured data $T_\mathrm{m}[i,j,k_\mathrm{m}]$ from their time-averages on July 31, 2014 (Thu.: working day). (a,b) Time series of $\tilde{T}[i,j,k]$. The domains encompassed by the broken lines are enlarged in the left-top subfigures. (c) Values of distance $\tilde{d}[i,j]$ between deviations $\tilde{T}[i,j,k]$ and $\tilde{T}_\mathrm{m}[i,j,k_\mathrm{m}]$ at W1, W3, and W6.

into P_human and D_eff expresses both of thermal and fluid effects. However, as shown in Figs. 10 and 11, the time-averages $\langle T\rangle$ and deviations $\tilde{T}$ in Case:3 are different from Case:1 and Case:2. In particular, the time-average $\langle T\rangle$ in Case:3 is smaller than Case:1. This phenomenon is newly observed with the current treatment in which the time-dependency of air motion is included via D_eff. Note that in many conventional analyses assisted by CFD program, the air motion in Eq. (1) does not change in time, and hence the effective diffusion in Eq. (5) becomes time-invariant. Even if ones prepare CFD-based sub-models for respective dynamic effects on in-room temperature due to buoyancy, mobile occupants, and so on, any superposition of these sub-models does not capture the dynamic effect by mobile occupants because of the time-dependency of air motion. The current modeling suggests for the first time that the time-dependent diffusion is crucial to understanding the spatio-temporal effects of human occupancy on in-room temperature distribution.

VI. CONCLUSION

This paper developed a method for modeling of in-room temperature distribution incorporated with human sensor data. The in-room thermal dynamics were simply modeled via a two-dimensional diffusion equation with effective coefficient. By incorporating human sensor data into the two terms $D_{\text{eff}}(\boldsymbol{x},t)\Delta T(\boldsymbol{x},t)$ and $P_{\text{human}}(\boldsymbol{x},t)$ of the equation, the so-called thermal and fluid effects by human occupancy were described. The modeling was applied to a practical office space in commercial building in Japan where human occupancy was measured in high resolution. Numerical simulations of the office space show that the modeling well reproduces the temporal changes of measured temperature without any consideration of air motion and captures the multiscale influence of human occupancy on in-room temperature distribution—the thermal and fluid effects. The computing time for the simulations also proves that the modeling realizes the fast prediction of the multiscale influence, which is not possible with CFD. Thus, we establish the effectiveness of the in-room temperature modeling that is computationally simple and physically accurate.

The modeling procedure is general and applicable to another office space where thermal dynamics in the horizontal (length and width) direction are dominant. Also, it is possible to quantify the thermal and fluid effects by other in-room heat sources and obstacle objects such as office equipment. That is, the modulating idea of D_{eff} is applicable to various indoor situations even if the condition (4) does not necessarily hold (see also App. A). Furthermore, the modeling procedure provides a new framework of the HVAC design and operation. One of the most relevant applications is the operational design of VAV systems. The VAV system includes two basic components [23]: central Air Handling Units (AHU) for heating or cooling and dispersed VAV units for air supply. The operation of a VAV unit changes D_{eff} and hence has an ability of controlling the multiscale effect reported in this paper. Here, for an office space where a VAV unit operates, the proposed model (5) becomes a *nonlinear* diffusion equation because the coefficient $D_{\text{eff}}(\boldsymbol{x},t)$ depends on the temperature $T(\boldsymbol{x},t)$, denoted as $D_{\text{eff}}(\boldsymbol{x},t,T)$. Thus, the nonlinear model is still simple compared with an ordinal CFD model and enables quantification of how the VAV operation dynamically responds to a change of the temperature distribution, thereby contributing to its operational design. In addition to the design, we contend that the modeling is applicable to real-time control of in-room temperature distribution with taking human occupancy into account. Conventional demand-controlled ventilation is based on information on human occupancy [6, 7] and has not used direct in-room temperature distribution for management of HVAC systems. The current model makes it possible to identify a dynamic response of fine-scale temperature driven by human occupancy and HVAC operation. Thus, as stated in Sec. I, by using the model output as a feedback signal, it becomes possible to design the HVAC management for local and precise regulation of the temperature $T(\boldsymbol{x},t)$ to a reference distribution $T_{\text{ref}}(\boldsymbol{x},t,N)$ that is a function of the human occupancy $N(\boldsymbol{x},t)$.

Finally, we conclude that the proposed modeling contributes to a *dynamics*-oriented approach to the HVAC design and operation, in contrast to the CFD analysis that mainly investigates detailed but *steady* thermal environment.

[1] J. L. M. Hensen and R. Lamberts, eds., *Building Performance Simulation for Design and Operation* (Spon Press, 2011).

[2] Z. Ren and J. Stewart, Energy and Buildings **35**, 257 (2003).

[3] W. Zhang, K. Hiyama, S. Kato, and Y. Ishida, Building and Environment **63**, 89 (2013).

[4] S. Osawa, S. Hara, K. Koga, M. Honda, and C. Kaseda, in *Proceedings of SICE Control Division Conference* (2013) in Japanese.

[5] R. Chintala, C. Price, and B. Rasmussen, ASHRAE Transactions **121**, 294 (2015).

[6] W. J. Fisk and A. T. D. Almeida, Energy and Buildings **29**, 35 (1998).

[7] M. J. Brandemuehl and J. E. Braun, ASHRAE Transactions **105** (1999).

[8] N. Li, G. Calis, and B. Becerik-Gerber, Automation in Construction **24**, 89 (2012).

[9] V. L. Erickson, M. A. Carreira-Perpiñán, and A. E. Cerpa, ACM Transactions on Sensor Networks **10**, Article 42 (2014).

[10] E. F. Camacho and C. Bordons, *Model Predictive Control: Second Edition* (Springer-Verlag London, 2007).

[11] Y. Ma, G. Anderson, and F. Borrelli, in *Proceedings of the 2011 American Control Conference* (IEEE, 2011) pp. 2089–2094.

[12] A. Afram and F. Janabi-Sharifi, Building and Environment **72**, 343 (2014).

[13] M. Kuki, H. Nakajima, N. Tsuchiya, and Y. Hata, in *Proceedings of 2013 IEEE International Conference on Systems, Man, and Cybernetics* (IEEE, 2013) pp. 4623–4628.

[14] Y. Agarwal, B. Balaji, R. Gupta, J. Lyles, M. Wei, and T. Weng, in *Proceedings of the 2nd ACM Workshop on Embedded Sensing Systems for Energy-Efficiency in Building* (ACM, 2010) pp. 1–6.

[15] V. L. Erickson, M. A. Carreira-perpiñán, and A. E. Cerpa, in *Proceedings of 10th IEEE Conference on Information Processing in Sensor Networks* (IEEE, 2011) pp. 258–269.

[16] G. J. Levermore, *Building Energy Management Systems: Applications to Low-energy HVAC and Natural Ventilation Control, 2nd Edition* (E & FN Spon, 2000).

[17] Y. Kono, Y. Susuki, M. Hayashida, I. Mezić, and T. Hikihara, IEICE Technical Report. NLP **114**, 1 (2014).

[18] G. A. Pavliotis and A. M. Stuart, *Multiscale Methods: Averaging and Homogenization* (Springer, 2008).

[19] M. Avellaneda and A. J. Majda, Communications in Mathematical Physics **138**, 339 (1991).

[20] S. B. Pope, *Turbulent Flows* (Cambridge University

Press, 2000).
[21] N. P. Gao and J. L. Niu, Indoor and Built Environment **14**, 5 (2005).
[22] J. Srebric, V. Vukovic, G. He, and X. Yang, Building and Environment **43**, 294 (2008).
[23] G. S. Okochi and Y. Yao, Renewable and Sustainable Energy Reviews **59**, 784 (2016).
[24] P. Holmes, J. L. Lumley, and G. Berkooz, *Turbulence, Coherent Structures, Dynamical Systems and Symmetry* (Cambridge University Press, 1996).
[25] X. Wu, B. W. Olesen, L. Fang, J. Zhao, and F. Wang, Energy and Buildings **112**, 141 (2016).
[26] J. W. Tang, Y. Li, I. Eames, P. K. S. Chan, and G. L. Ridgway, Journal of Hospital Infection **64**, 100 (2006).
[27] S. Kato, H. Kobayashi, and S. Murakami, Transactions of the Society of Heating, Air-Conditioning Sanitary Engineers of Japan **69**, 39 (1998), in Japanese.
[28] I. Mezić, J. F. Brady, and S. Wiggins, SIAM Journal on Applied Mathematics **56**, 40 (1996).
[29] F. Kreith, ed., *Fluid Mechanics* (CRC Press, 2000).
[30] S. Murakami, S. Kato, and J. Zeng, Building and Environment **35**, 489 (2000).
[31] I. Mezić and A. Banaszuk, Physica D: Nonlinear Phenomena **197**, 101 (2004).
[32] A. Fannjiang and G. Papanicolaou, SIAM Journal on Applied Mathematics **54**, 333 (1994).
[33] Y. Kaneda, Physics of Fluids **29**, 701 (1986).
[34] K. Yoshida, T. Ishihara, and Y. Kaneda, in *Statistical Theories and Computational Approaches to Turbulence: Modern Perspectives and Applications to Global-Scale Flows*, edited by Y. Kaneda and T. Gotoh (Springer, 2003) pp. 219–228.
[35] ASHRAE, "ASHRAE Handbook: Fundamentals," (1985).

Appendix A: Extension of modeling in time-invariant coefficient $D_{\rm eff}^{(0)}$

This section shows the possibility to extend the modeling in the time-invariant coefficient $D_{\rm eff}^{(0)}$, which is established under the condition (4), to more general situations. If the temporal average in Eq. (4) is not zero, then the diffusion coefficient becomes time-varying, denoted as $D_{\rm eff}^{(0)}(\boldsymbol{x}, t)$. This situation may occur when multiple VAV units are operated in an office space and produce a local, non-advective flow. Also, if the spatial average in Eq. (4) is not zero, then the homogenization-based equation (5) includes the advection term. Here, the modulation idea of $D_{\rm eff}^{(0)}$ is effective in the above two situations. In the former, the VAV units would change the total energy of the fully-developed turbulent flow in Ω, namely its energy spectrum. Simultaneously, the energy spectrum is changed by the local effect by a mobile occupant. Both the changes are approximately represented by an extension of the modulation formula like $D_{\rm eff}^{(0)}(\boldsymbol{x}, t)\{1 + \varepsilon N(\boldsymbol{x}, t)\}$. Also, in the latter situation, the local effect does not influence the emergent advective flow over Ω because of the well-established phenomenology of energy cascade. Thus, the modulation formula $D_{\rm eff}^{(0)}(\boldsymbol{x})\{1 + \varepsilon N(\boldsymbol{x}, t)\}$ is enough to the latter situation.

Appendix B: Derivation and identification of $D_{\rm eff}^{(0)}$

This section explains formula and value of the nominal effective diffusion coefficient $D_{\rm eff}^{(0)}$ from a velocity profile of air motion. They are based on the two following physical mechanisms: eddy diffusion behavior under a homogeneous turbulent flow [20] and effective diffusion behavior under a homogeneous large-scale flow [19, 32].

First, we derive the formula of eddy diffusivity $D_{\rm eddy}$ under the homogeneous turbulent flow. Now, we use L_0 to represent the length-scale of the averaged velocity $\boldsymbol{u}_0$. It is thus known that the time-varying component $\tilde{\boldsymbol{u}}$ contains *small-eddy* components whose length-scales are smaller than L_0. Heat transfer by these small-eddy components is often modeled as isotropic diffusion, called eddy diffusion. This idea is widely known in *large eddy simulation*: see e.g. [20, 33]. In particular, Yoshida, *et al.* [34] addressed the fluid components with length-scales smaller than a cut-off scale $L_{\rm c}$ and modeled its contribution to the heat transfer as the eddy diffusivity $D_{\rm eddy}$. The formula of $D_{\rm eddy}$ is presented in [34] as follows:

$$D_{\rm eddy} = \left(\frac{U_0^3}{L_0}\right)^{1/3} L_{\rm c}^{4/3}, \tag{B1}$$

where U_0 stands for the characteristic scale of the averaged velocity $\boldsymbol{u}_0$. It is shown in [34] that Eq. (B1) is valid if $L_{\rm c}$ is smaller than the half of the target length-scale L of heat transfer of interest.

Next, we look at the contribution of $\boldsymbol{u}_0$ and of the residual large-scale components of $\tilde{\boldsymbol{u}}$ which length-scales are larger than $L_{\rm c}$. Ceiling air outlet generates spatially-symmetric convection cells with respect to an outlet duct [4, 35]. Thus, when the outlet ducts are homogeneously located, $\boldsymbol{u}_0$ is expected to exhibit a spatially-periodic flow structure similar to the Rayleigh-Bénard convection. Because of the spatial-periodicity of $\boldsymbol{u}_0$ and homogeneity of $\tilde{\boldsymbol{u}}$, the contribution is represented as a diffusion term described by a second-order, skew-symmetric, and spatially-periodic tensor, called *diffusion tensor*. The tensor is then homogenized into an isotropic *effective diffusion* term [19, 32]. The homogenization is described in the next paragraph. Now, let us introduce a constant coefficient $D_{\rm large}$ to quantify the pure-contribution of the components with length-scales in the interval $[L_{\rm c}, L_0]$, which does not include contribution of the small-eddy components. The coefficient $D_{\rm large}$ is written via dimensional analysis as follows:

$$D_{\rm large} = L_{\rm large} U_{\rm large}, \tag{B2}$$

where $L_{\rm large}$ and $U_{\rm large}$ are the characteristic length and

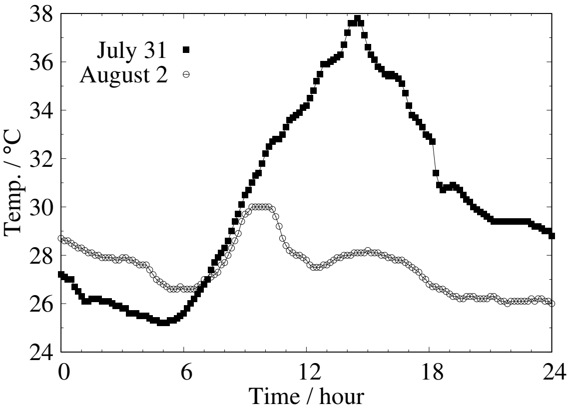

FIG. 12. Outdoor temperature data $T_{\rm out}$ measured on July 31 and August 2, 2014 (Thu. and Sat.).

velocity of the diffusive contribution given as

$$L_{\rm large} = \frac{2}{1/L_0 + 1/L_{\rm c}}, \tag{B3}$$

$$U_{\rm large} = \left(\frac{U_0^3}{L_0}\right)^{1/3} \sqrt{\int_{1/L_0}^{1/L_{\rm c}} k^{-5/3}{\rm d}k}, \tag{B4}$$

where k is the wavenumber of flow. Eq. (B3) implies that the averaged wavenumber $1/L_{\rm large}$ in the interval $[1/L_0, 1/L_{\rm c}]$ is adopted as the characteristic wavenumber of the target heat transfer. Also, Eq. (B4) is derived with the kinetic energy contained in the interval $[L_{\rm c}, L_0]$ under the assumption that the spectrum of kinetic energy obeys the Kolmogorov's minus five-thirds law [20]. The square root in Eq. (B4) is introduced to associate the kinetic energy with the velocity in terms of dimensional consistency.

Finally, we construct the formula of $D_{\rm eff}^{(0)}$ by combining the contributions of $D_{\rm eddy}$ and $D_{\rm large}$ to heat transfer. The constant $D_{\rm eddy}$ corresponds to the diagonal elements of diffusion tensor, which contribute the heat transfer on small scale, and $D_{\rm large}$ to the non-diagonal elements, which contribute the heat transfer on large scale. The tensor is homogenized into diagonal effective tensor through the standard asymptotic expansion, and the bounds of elements of the homogenized tensor are given as geometric average of elements of the diffusion tensor [19, 32]. Note that the effective tensor is isotropic in the target space because of the two reasons. First, the outlet ducts of HVAC units are homogeneously located along both length and width of the target space (see Fig. 1(c)); Second, the outlet volume per one duct is almost uniform (see Fig. 1(c) and Tab. I). Therefore, we formulate the nominal coefficient $D_{\rm eff}^{(0)}$ as follows:

$$D_{\rm eff}^{(0)} = \sqrt{D_{\rm eddy} D_{\rm large}}. \tag{B5}$$

In this paper, the length-scale L of heat transfer is set at $\Delta x = \Delta y = 1.8\,{\rm m}$, and the cut-off scale $L_{\rm c}$ at $L/2 = 0.9\,{\rm m}$ for validity of Eq. (B1). By substituting the values of L, $L_{\rm c}$, L_0, and U_0 into Eqs. (B1)–(B5), the nominal value of $D_{\rm eff}^{(0)}$ is calculated as $1.2\,{\rm m}^2/{\rm s}$.

Appendix C: Outdoor temperature data $T_{\rm out}$

Figure 12 shows the outdoor temperature data $T_{\rm out}$ on July 31 and August 2, 2014 (Thu. and Sat.). For the target period 9:00 to 18:00, the temperature is higher than the outlet one of HVAC units (see Tab. III). The high temperature enhances the thermal load $P_{\rm conv}$ and then cancels the cooling input from HVAC units. This is a quantitative evidence that the in-room temperature shown in Figs. 3, 7, and 8 is higher than the outlet one.

Appendix D: Discretized formulation of $P_{\rm solar}$

This section provides a formulation of the heat input $P_{\rm solar}$ from solar radiation in the target space. The heat input $P_{\rm solar}$ is assumed to be spatially uniform in the target office space and given in [1] as follows:

$$P_{\rm solar}[k] = K_{\rm solar} \frac{P_{\rm m}[k] S_{\rm wind}}{144 h \Delta x^2}, \tag{D1}$$

where $P_{\rm m}$ stands for the solar radiation through windows per unit area and time, and $S_{\rm wind} = 44.8\,{\rm m}^2$ for the total area of the eastern windows. The denominator of right-hand side of Eq. (D1) coincides with the total volume of the target three-dimensional object. The coefficient $K_{\rm solar}$ is introduced to represent the solar shading by louvers and blinds, and its practical value is 5.1×10^{-2} [1].

Appendix E: Estimation of $K_{\rm conv}[i_{\rm b}, j_{\rm b}, k]$

By using the so-called overall heat transfer coefficient U shown in Tab. II, we provide an estimation of the convection coefficient $K_{\rm conv}[i_{\rm b}, j_{\rm b}, k]$. Here, the overall heat transfer per volume at boundary node $[i_{\rm b}, j_{\rm b}] \in \partial A$ is represented as follows:

$$\begin{aligned} U[i_{\rm b}, j_{\rm b}] & \frac{T_{\rm ext}[k] - T[i,j,k]}{\Delta x} \\ &= U[i_{\rm b}, j_{\rm b}] \frac{T[i_{\rm b}, j_{\rm b}, k] - T[i,j,k]}{K_{\rm conv}[i_{\rm b}, j_{\rm b}, k] \Delta x^2} \qquad \text{(E1)} \\ &= \rho c_{\rm p} D_{\rm eff}[i,j,k] \frac{T[i_{\rm b}, j_{\rm b}, k] - T[i,j,k]}{\Delta x^2}, \qquad \text{(E2)} \end{aligned}$$

where we used Eq. (19) for deriving the right-hand side of Eq. (E1) and also used a discretized diffusion term of Eq. (5) at node $[i, j]$ for deriving the right-hand side of Eq. (E2). The right-hand sides of Eqs. (E1) and (E2) lead to the formula of $K_{\rm conv}$ in Eq. (20).